SMALL SPACECRAFT FOR PLANETARY EXPLORATION

Eric Shear

A Thesis submitted to the Faculty of Graduate Studies in Partial Fulfillment of the Requirements for the Degree of Master of Science

Graduate Program in Earth and Space Science, York University, Toronto, Ontario

December 2017

Abstract

After an overview of the progress that have been made in small spacecraft for planetary exploration, two planetary mission studies utilizing small spacecraft technologies are presented. HYPATIA is a proposed mission that would demonstrate the use of planetary balloon and water electrolysis technology on the Martian northern polar cap. The combination of both technologies allows a small science payload to be landed repeatedly and carried across the polar terrain. HYPATIA consists of a small gondola under a metallised Mylar balloon filled with hydrogen from the polar ice. SIREN is a proposed mission concept that would demonstrate the use of small spacecraft at the rings of Saturn to quantify the ring environment and study the composition and dynamics of the ring particles. SIREN consists of several daughtercraft deployed from and networked to a mothership in hover-orbit over the ring plane. Many existing small spacecraft technologies are leveraged to make these missions possible.

Acknowledgments

I would like to thank Dr. John Moores for his endlessly helpful advice on both projects that ended up in this thesis, as well as for giving me the opportunity to work with him during the last summer of my undergraduate career at York University on the Mars solar balloon project that eventually led to HYPATIA.

Several members of the Planetary Volatiles Laboratory were kind enough to offer help on various roadblocks I encountered during the research process. Dr. Abdelkrim Toumi, Brittney Cooper, Casey Moore, and Elisabeth Smith looked over my Matlab scripts to help me narrow down errors that were keeping me from getting the right results.

Several other people should be mentioned for the additional feedback they offered on the HYPATIA concept after it passed peer review. Julian Nott, from his extensive ballooning experience, had a dim opinion of Martian conditions. His tough critique of HYPATIA forced me to refine the concept with updated knowledge of the Martian polar winds, with the help of Dr. Isaac Smith. A few veterans of the JPL balloon experiments in the 1990s, Jim Cantrell, Louis Friedman, and Viktor Kerzhanovich, informed me that a snake guiderope would work on a balloon. One final thanks should be extended to Dr. Ellen Stofan and Dr. Ralph Lorenz for putting me in touch with the Mars ballooning experts.

A few planetary science and space engineering experts gave some of their time to review my SIREN draft during the peer-review process - Matthew Tiscareno, Barbara Cohen, Linda Spilker, and Matt Hedman.

Table of Contents

List of Tables

List of Figures

1: Introduction

1.1 The Value of Small Spacecraft for Planetary Exploration

Over the last 52 years, from Mariner 4 to Juno, interplanetary exploration has generally relied on spacecraft massing over 200 kilograms. Technological advances have shrunk the mass, volume, and power requirements of space hardware, allowing greater percentages of the mass of successive spacecraft to be devoted towards scientific payloads. In recent years, these same advances have also made possible several interplanetary spacecraft with masses well below 200 kilograms, without diluting capability.

1.1.1 Small spacecraft for planetary science

Small spacecraft have proliferated in recent years, largely due to the CubeSat standard [1], invented in 1995 at Stanford University and California Polytechnic Institute. A CubeSat is a miniaturized spacecraft that is made up of multiples of units with dimensions of $10 \times 10 \times 10$ cm. A 1U CubeSat consists of only one unit, with a maximum mass of 1.33 kg [2]. Each unit can be stacked together to accommodate larger payloads or more hardware, resulting in configurations from 2U to 6U or greater.

This trend has sparked interest in using small spacecraft to accomplish scientific objectives that are impractical for larger spacecraft, such as cheap sacrificial probes, multi-point swarm measurements, and low-gravity landers [3]. For planetary science, the potential exists for using CubeSats and other smallsats for networked observations, sacrificial missions, and secondary payloads on larger spacecraft for increased science return at a reasonable cost. These new mission classes offer lower costs and risk mitigation for some types of scientific observations, and make new ones possible [3]. They may also fulfill some of the priorities listed in the 2013-2022 Planetary Science Decadal Survey.

Opportunities exist for stand-alone small spacecraft missions, but in this regime excess launch performance can accommodate additional smallsats as secondary payloads on the primary spacecraft. The Exploration Mission-1 (EM-1) test flight of the Space Launch System in 2018 is one such example. It will include several slots for planetary CubeSats for lunar orbit and other destinations [4].

1.1.2 State of the art of small planetary spacecraft

Interplanetary space is more challenging than Low Earth Orbit (LEO) for small spacecraft due to their lack of internal volume, which makes thermal control design more difficult by limiting the area for heating elements and radiators. It also limits the redundancy available to make the spacecraft resistant to cosmic radiation. Despite these challenges, there are ways to make CubeSats more competitive in interplanetary applications, such as rigorously testing commercial off-the-shelf (COTS) components to mitigate risk [5].

Several interplanetary CubeSats are under development. INSPIRE (Interplanetary Nano-Spacecraft Pathfinder in Relevant Environment) from NASA Jet Propulsion Laboratory is a pair of 2U CubeSats for measuring the fine-scale structure of the solar wind at 150 million kilometers from Earth [6]. The NASA/JPL InSight lander will have two 6U CubeSats, collectively called Mars Cube One, to relay communications during the entry and landing phase. This capability is not mission-critical for InSight, but the success of Mars Cube One will validate further CubeSat applications for exploring the solar system [7]. Another 6U CubeSat planetary spacecraft under development is the Near Earth Asteroid (NEA) Scout mission to be launched as a secondary payload on the EM-1 test flight in 2019. It is defined as a solar sail demonstrator and asteroid prospector [8]. NASA has also selected a few lunar CubeSat missions, including Lunar Flashlight [9] and Lunar IceCube [10], as secondary payloads on the EM-1 test flight. Whether or not EM-1 launches by this date remains to be seen.

1.1.3 CubeSat longevity and reliability

CubeSats are generally perceived as suitable only for short, low-value demonstration flights. This is rooted in a bias towards the exceptionally conservative methods traditionally employed by the aerospace industry, which favor redundancy and reliability models over actual flight history. This has changed in recent years due to shifts in industry thinking, as shown by the NASA CubeSat missions detailed in the previous section. This shift was triggered by the proliferation of large numbers of quality space-grade parts available commercially, which has resulted in the capability to get quality and reliability information that cannot be obtained from any amount of testing on a small number of parts [5].

Over the last 20 years, most CubeSat failures have come from insufficient system testing or being launched into an unexpected environment it was not designed for, often due to a failure in the launch vehicle. Generally, the more resources the organization has to spend on spacecraft development, the more successful its spacecraft will be. Between 1981 and 2003, about half the university CubeSats that were launched remained operating up to or past their design lifetimes [11].

1.2 Mission proposals

This thesis will cover two proposals for small planetary missions to Mars and the Saturnian system that have not been previously described in the literature. Both mission proposals are designed to carry out objectives that would be impractical for larger spacecraft/rovers to achieve, either on their own or piggybacking on larger spacecraft to access areas that are otherwise inaccessible for increased science return.

1.2.1 HYPATIA

The first concept, Hydrolyzed Polar Terrain Ice Aerobot (HYPATIA), is an ultralight balloon mission on the Martian northern polar layer deposit (NPLD). It takes advantage of the katabatic wind, generated by the fixed temperature of saturated air over 200 K ice and local topography, to transverse approximately 500 kilometers from the NPLD center to its rim. It would vent some of its lifting gas to land on the equatorial-facing slope in each of the spiral troughs, where the ice and dust layers are exposed. The low buoyancy of the Martian atmosphere places severe constraints on a balloon’s allowable mass, so this vehicle carries only a minimum of scientific instruments sufficient for sampling the polar ice at each site.

1.2.2 SIREN

The second case study, Saturn Ice Ring Exploration Network (SIREN), is a constellation of small spacecraft deployed from a mothership to study the A and B rings, the most dense, ice-rich rings around Saturn. Each daughtercraft is a node in the network, carrying a few instruments to analyze/sample a single feature of the ring environment, from local magnetic gradients to impurities in each ice boulder. The small size of each daughtercraft allows them to approach the ring plane itself and navigate more easily among the ice boulders for sampling operations. The mothership keeps each daughtercraft recharged and heated, and stores their crosslinked data for later downlink to Earth at high data rates. The synergy between the mothership and the daughtercraft leads to much greater science return than a single spacecraft of equivalent mass, making this concept a possible improvement on the earlier Saturn Ring Observer (SRO) concept.

1.3 Science objectives and requirements

In this section, the science objectives and requirements of each mission are shown in order to inform their design strategy in Section 1.4. The tool of choice is a science traceability matrix, which is used in NASA planetary mission proposals in order to clarify how the mission will accomplish its science objectives, and how these objectives relate to goals set at the higher level. A STM shows the relationship between mission objectives, science objectives, measurement objectives, and instruments. [12].

1.3.1 HYPATIA

The goal of HYPATIA is to understand the large-scale climatic record over the past 10^6 years of Martian history, as preserved in the northern polar layer deposit (NPLD). This is done by sampling and imaging the stratigraphic layers exposed on the leeward side of the spiral troughs. A secondary goal is to monitor the weather on the NPLD surface, for both scientific and engineering data. These goals are broken down into a few science objectives, which then flow into the other objectives and requirements as shown in Table 1.1:

Table 1.1: HYPATIA Science Traceability Matrix

Science Objectives	Measurement Objectives	Instruments
Characterization of the stratigraphic layers	Context imaging	Nadir imager
	Element and isotopic abundance and ratio measurement (D/H, O-16/O-18, CHNOPS)	Tunable laser spectrometer
Understand weather processes	Altitude & pressure measurement	Air pressure sensors
	Wind direction measurement	Wind velocity sensors
	Air temperature measurement	Air temperature sensors
	Measurement of infrared flux radiated from surface	Ground temperature sensor
	Measurement of water exchange between surface and atmosphere	Relative humidity sensor

1.3.2 SIREN

The goal of SIREN is to understand how the Saturnian rings formed and evolved, by imaging and sampling the ice particles in the A and B rings. A secondary goal is to improve on Cassini's measurements of the magnetosphere in the vicinity of the rings, by spending more time within the ring plane and closer to the rings than Cassini did. These goals are broken down into a few science objectives, which then flow into the other requirements as shown in Table 1.2:

Table 1.2: SIREN Science Traceability Matrix

Science Objectives	Measurement Objectives	Instruments
Characterization of ring particle dynamics	Measure relative velocities	Visible imager
Characterization of magnetic field environment	Measure magnetic field gradients	Magnetometer
	Measure abundance of ions and neutral particles	Ion and neutral mass spectrometer
Characterization of impurities & isotopes in ice particles	Surface impurities	Alpha particle X-ray spectrometer
	Deuterium/hydrogen and O-16/O-18 abundances and ratio measurement	Tunable laser spectrometer

1.4 Design strategy

Both mission proposals were designed with a combined top-down, bottom-up strategy that took in account their objectives, environments, and available technologies. Each strategy has its pros and cons, so care was taken to blend both approaches to obtain the most optimal results.

1.4.1 Top-down design

A top-down approach starts with the big picture and breaks that down into smaller segments. In space mission design, this means starting with the objectives of the mission, and identifying the constraints from its intended environment that will govern the design. From these pieces of information, the requirements of each subsystem are identified. For this reason, this approach lends itself well to large, complex projects with many custom-designed components such as a new spacecraft. By imposing constraints that trickle down to the most basic elements of the system, this approach has the potential to control costs, but may fail if the model doesn't include enough detail to be realistically validated. In such a case, redesigning the components will lead to cost overruns [13].

1.4.2 Bottom-up design

In spacecraft design, a bottom-up approach is used when the individual components are known in detail and are available for selection. This can reduce cost and development time because the components have known operational tolerances and don’t need extensive testing for the environments they are designed for. They are known as commercial off-the-shelf (COTS) components and are often used in CubeSats for cost reasons. Bottom-up design pieces these components together to create a more complex system, but carries the risk of ending up with isolated and locally optimized components at the expense of a less optimized system. Without top-down oversight, this approach can fail if there is insufficient system-level testing to validate the entire spacecraft before launch [13].

1.4.3 Integrated strategy

In many cases, a blend of both approaches produces the most optimal results. This integrated approach was used for both HYPATIA and SIREN. A spacecraft, especially a small, highly integrated one such as a CubeSat, requires an approach that is mostly top-down but usually benefits from a locally bottom-up approach for known components.

For HYPATIA, the process started with a study of the Martian atmosphere at the poles. It was soon discovered that the low density of the Martian atmosphere led to a weak lifting force even with hydrogen lifting gas and so a decision was made to keep the floated mass as low as possible to keep the balloon parameters from becoming unwieldy. This decision flowed down to the payload instrument selection, which was carried out according to the science requirements and to keep the total instrument mass as low as possible. From there, the resulting payload imposed bottom-up requirements on the gondola structure, and the power, thermal control, and communications subsystems.

For SIREN, the overarching requirement was to not exceed 10 kg for all daughtercraft, since increased mass requires increased thrust for the same acceleration. The 10-kg requirement was chosen after surveying each CubeSat variant from 2U to 6U, and deciding on the 6U because it offered the most payload volume for the existing instruments that were selected from the bottom up.

1.5 Scope and limitations of study

All planetary missions, regardless of the size of the spacecraft being flown, are collaborative efforts involving hundreds of people. This is due to the complexity of each spacecraft and their operations. This thesis was meant to provide a high-level overview of two planetary missions with small spacecraft and to identify their physical limits, without delving into the blueprints of each subsystem. It falls to other researchers to analyze the findings of this thesis and use it as a starting point to expand on or critique the HYPATIA and SIREN designs.

1.5.1 Significant figures

For most calculations in this thesis, the number of significant figures in the answer was based on the least known input parameter. In HYPATIA's case, the katabatic wind speed is not known within to more than one significant figure, so that resulted in the estimated travel distance having only one significant figure. The theoretical calculations for the scale height and pressures relied on quantities that are known within several significant figures. The results of these calculations were used to inform the amount of mass that can be floated with a balloon as accurately as possible.

The orbital calculations for SIREN (Chapter 3) were meant to find very small Δvs on the order of cm/s or mm/s, so to obtain the most precise results, the number of significant figures was not reduced.

1.5.2 CAD modeling

All CAD models in this thesis were done in OnShape, a cloud CAD suite that is accessible through any internet browser. Every effort was made to discover the dimensions of each component (Section 1.5.3) that goes into each proposed spacecraft, so they could be modeled in OnShape. The intention was to see how each component fit together in assemblies, in order to discover areas of overlap and empty volumes that can be used for system integration. Beyond the initial modeling process, no effort was made to design each component down to the last nut and bolt, since this is only the beginning of the mission design process.

1.5.3 Current and near-term hardware

This study focused on existing and near-term hardware to reduce the number of unknowns in each mission design. The "near-term" descriptor refers to hardware that has been validated in laboratory tests, but not yet flown. In NASA parlance, they are called "mid-TRL (Technology Readiness Level)" hardware, while existing hardware is called high-TRL [14]. No effort was made to assume or predict the capabilities of future (low-TRL) hardware that has not yet been tested, except in the discussion sections of Chapters 2 and 3, and in Chapter 6, which deals with future work. Basing the mission designs on mid- and high-TRL hardware allows for capability growth and cost estimation confidence as they mature.

1.5.4 Focus on small spacecraft

Both case studies focus on small spacecraft (within the 10-kg mass range) and not on any larger spacecraft that would support them, such as an orbiter for HYPATIA and the mothership for SIREN. They are treated as mostly outside the scope of this thesis, except in areas where they would support the spacecraft being studied. For instance, the Mars Reconnaissance Orbiter is only relevant in that it is in the right orbit to serve as a communications relay between HYPATIA and mission control. The SIREN mothership was not studied to the same extent as its daughtercraft, except in areas where it would support the network.

2: Hydrolyzed Polar Terrain Ice Aerobot (HYPATIA)

2.1 Overview

2.1.1 Balloons for planetary science

Balloons have been long recognised as unique scientific platforms due to their ability to rapidly perform high-resolution imaging and *in-situ* measurements over large distances with low power consumption. They have been proposed for a limited number of niche mission scenarios where controllability and specificity of location are not important. Unfortunately, these platforms suffer from relatively short operational lifetimes and relatively low payload mass limits.

For planets with optically thin atmospheres, imaging from balloons has been supplanted by sub-metre per pixel orbital imaging [15]. However, a strong case for balloons remains where *in-situ* measurements are required over large areas. Several groups have made the case for balloon-deployed instruments in the planetary context. For instance, the Jet Propulsion Laboratory has proposed a 20-kg sounding radar similar to SHARAD on Mars Reconnaissance Orbiter for use on a Mars balloon. Another balloon proposal was to re-fly the 5-kg gamma ray spectrometer that was used on Mars Odyssey [16]. The goal of both proposals was to fly these instruments at a lower altitude, where they could image the surface and subsurface at higher resolutions than what would be possible from orbit.

2.1.2 State of the art of Martian balloons

Mars is the most challenging environment in which to float a balloon vehicle, due to the limited buoyancy available in its low-density atmosphere. This forces the use of very large envelopes when compared to balloons deployed to other atmospheres in the solar system. While using miniaturised electronics and low molecular-weight lifting gases can mitigate the low buoyancy of the Martian atmosphere, there is still a fundamental limit to how much mass can be floated.

Balloons can be scaled up to fly heavier payloads, but a larger balloon takes longer to deploy, which is an added risk during the entry, descent, and inflation (EDI) phase. Experiments conducted by Jet Propulsion Laboratory on helium balloon deployment in Earth's stratosphere, where the pressure is similar to that on Mars, confirmed that a spherical balloon 10 metres in diameter can be aerially deployed within 90 seconds. This balloon had a total mass of 7.4 kg, and its envelope was polyester with a thickness of 12.7 μm. It was initially moving at a speed of 25 m/s [17]. The rest of this chapter will assume similar numbers in order to keep the following proposal plausible.

2.1.3 Ballooning opportunities on the Martian polar caps

One such appealing niche is the exploration of the north polar layered deposits (NPLD) of Mars. The NPLD is very broad, of order 1,000 km, and is accessible for less than a quarter of the Martian year (Ls = 90° to 180°) due to seasonal CO_2 ice sublimation. Exploring the NPLD in this amount of time is impractical with a rover, but is conducive to a balloon. The highest point of this formation is in the approximate centre, near 90° N, and its lowest points are along the rim, generating katabatic winds from the cold air flowing down and outwards from the centre which could propel the balloon on its journey. Along the way, the aerobot could replenish its hydrogen lifting gas via *in-situ* electrolysis of the exposed water ice [18].

This chapter will present a potential mission concept to advance Mars polar science using a small gondola suspended under a hydrogen balloon. The gondola would be equipped to image the polar terrain, take atmospheric measurements, and to analyse the evolved gases from the ice at multiple different sites.

2.2 In-situ sampling of the Martian NPLD

2.2.1 Scientific value of the Martian NPLD

Orbiting spacecraft since Mariner 7 have revealed the PLDs to consist of a CO_2 ice layer in winter, which sublimates every spring to reveal a smaller permanent water-ice layer. During each winter, 25% of the atmosphere freezes out on the PLDs and as far as 60°N, trapping dust and trace gases within their stratigraphic layers [19]. On longer timescales, the trapped dust and gases are thought to vary in concentration across stratigraphic layers, according to periodic variation in climate caused by secular changes in the orbit and obliquity of Mars. The PLDs thus offer an accessible record of Martian climate history for at least the past $\sim10^6$ years [20].

The fixed temperature of saturated air over 200 K ice, combined with the local topography, gives rise to katabatic winds flowing downwards and outwards from the high centre to the low rim. This behaviour, coupled with Coriolis rotation, causes a pinwheel pattern of spiral troughs on the NPLD [21]. The stratigraphic layers are exposed on the equatorial-facing slopes due to wind erosion, with the same wind depositing the removed material onto the pole-facing slopes [22]. The exposure of these layers creates an opportunity to investigate the climactic history of Mars at low cost. Additionally, as with terrestrial ice cores, inclusions trapped in the near surface ice may give clues to the geological and biological history of Mars [23] as well as a record of solar insolation that could inform terrestrial climate studies.

2.2.2 Necessary in-situ activities

To date, no probe has visited the PLDs of Mars. As a result, there is no ground truth to examine whether orbital imagery of layers correlate with variations in ancient climate. Isotopic ratios, in particular the deuterium/hydrogen (D/H) and $^{16}O/^{18}O$ ratios, in each layered deposit may provide clues to how water was exchanged between the polar caps and the atmosphere, and the isotopic character of previous atmospheres [24]. Furthermore, within the present cap, there are at least three different historical caps, each exposed in a different area [25]. A mission capable of investigating the exposed historical remnants in a single launch would be able to see if there are any major shifts in the isotopic character of the atmosphere on Ma-timescales. Such variations could be examined by an instrument sensitive to different isotopologues of water, for instance, a sensitive quadrupole mass spectrometer or a tunable laser spectrometer.

2.2.3 Hopping balloon vs. rover

The permanent NPLD is 1,000 kilometres across. A long-distance sampling vehicle would need to transverse at most 500 kilometres from the centre to the rim, in order to fulfill the scientific requirements outlined in Section 2.2.2. There are two options for the proposed vehicle: a wheeled rover and a balloon that lands and takes off repeatedly using hydrogen sourced from polar ice. Both options are severely constrained by the crocus date. The NPLD is not free of CO_2 ice until after the summer solstice. This reduces the effective mission duration to about 126 sols, from the summer solstice to a point when the sun begins to cross the horizon.

Assuming the maximum drive progress of the Lunakhod Rover of 16.533 km in just 12 days in 1973, approximately 1.378 km per day [26], a rover would be limited to a traverse of no more than 178 km. However, the Lunakhod rovers were tele-operated, a mode of operations not possible on Mars, given the light-time delay. While advances in autonomous navigation will increase the total distance that may be covered in a single sol and the terrain of the NPLD is easier to traverse than the terrain at lower latitudes [27], typical distances of the current Mars Rovers, such as the Mars Science Laboratory, of 100–200 m per sol are more realistic. When also considering the time required to perform scientific analysis, the distances traversed by modern spacecraft suggests that rovers are limited to at most a few tens of kilometres of traverse distance.

A hopping balloon offers a different sampling strategy. The katabatic wind is at least 6 m/s. At this speed, a balloon vehicle can cross approximately 500 kilometres in 24 hours. There is thus ample margin for surface operations before the timeline runs out of uninterrupted sunlight. This vehicle can be used to investigate the exposed areas of the historical remnant deposits within a single mission duration, at the cost of fewer coring sites per slope.

2.3 Mission profile

2.3.1 Concept

The mission profile concept is shown in Figure 2.1. HYPATIA is small enough to be either a stand-alone mission or to share a spacecraft with a dedicated polar orbiter/lander. In either case, the aerobot is encased inside its own aeroshell for atmospheric entry. Following launch (Figure 2.1, Panel 1), the spacecraft enters a direct trajectory to Mars. During cruise, the aerobot is dormant except for periodic health-check wakeups commanded by the cruise stage electronics.

At Mars arrival, the capsule intersects the atmosphere at polar latitudes. The capsule decelerates using an ablative heat shield until it achieves terminal velocity in the vertical direction and mean atmospheric velocities in the horizontal direction. At this point, a parachute is deployed to further slow the aerobot down until it can deploy its balloon from a pressurised hydrogen bottle. The bottle is then dropped and the aerobot allowed to descend until it reaches equilibrium at a low altitude over the northern PLD.

Figure 2.1 HYPATIA mission profile (see online version for colours)

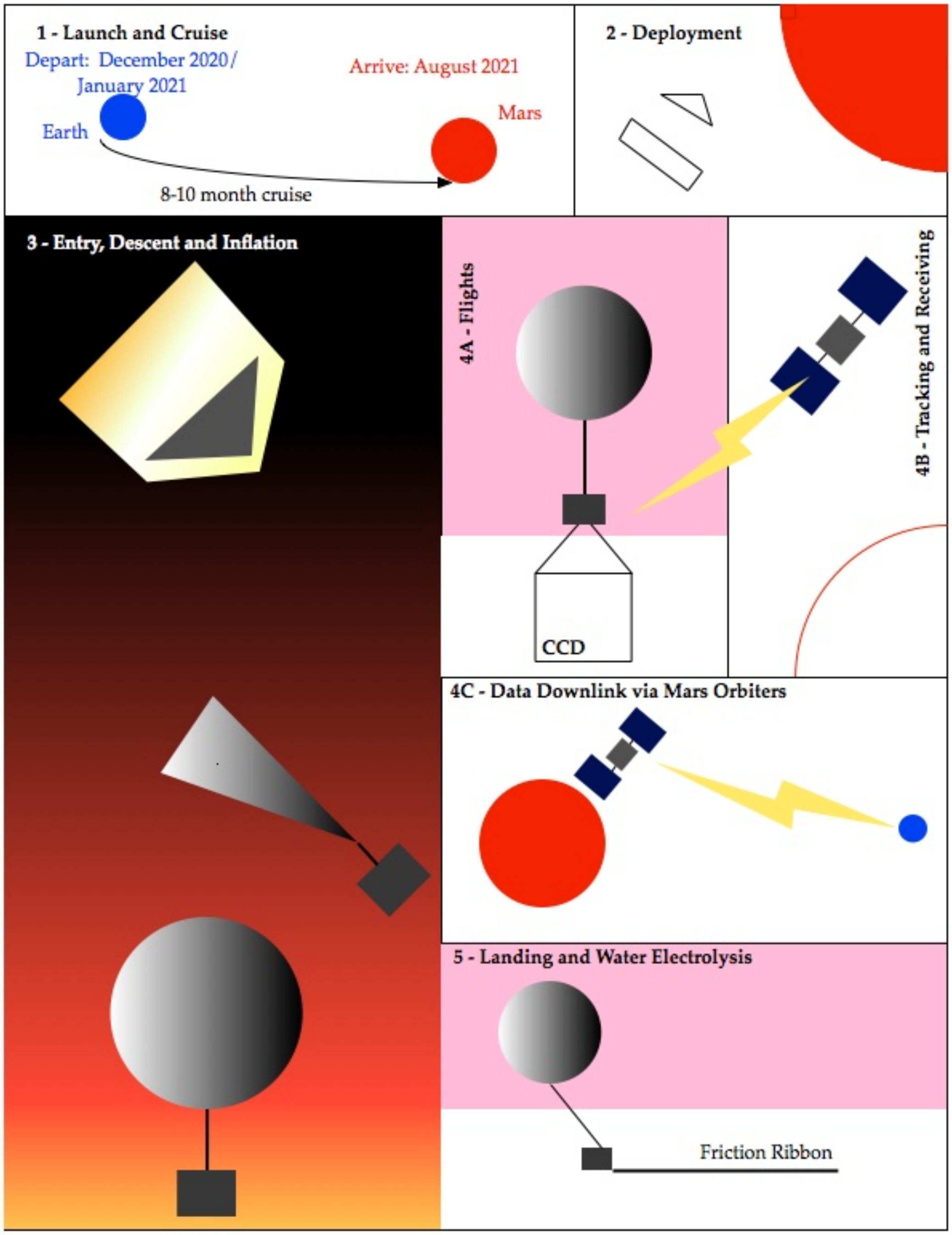

Notes: Beginning with launch and cruise (1), the atmospheric entry capsule (triangle) separates from the cruise stage (2) prior to atmospheric EDI (3). During flight (4A), the vehicle takes images of the polar terrain and atmospheric measurements before uplinking the data to an orbiter (4B), which then relays it back to Earth (4C). Meanwhile, the balloon vehicle conducts its own autonomous landings with the help of a high-friction ribbon on the ice, using water electrolysis to replenish its supply of hydrogen lifting gas (5).

The aerobot begins its mission near the north pole and travels with the katabatic wind, stopping at each equator-facing spiral trough. It descends by venting some of its lifting gas, to the point where the gondola can grip the ice with the assistance of a high-friction rubber ribbon. The gondola carries a thermal drill to bite into the ice and sublimate it in the low atmospheric pressure, at which point the water vapour self-pressurises and condenses inside the gondola. The liquid water is fed into the electrolysis stack, where it is split into hydrogen and oxygen. The oxygen is vented, and the hydrogen is pumped into the balloon envelope where it replaces the gas lost during the descent. During this process any dissolved species in the water are analysed with a small spectrometer. The science payload is further enhanced with instruments for atmospheric readings and imaging the polar surface during flight.

Meanwhile, the data is relayed back to Earth via one of the existing Mars orbiters or a dedicated communications relay satellite with an inclination high enough to establish line-of-sight with HYPATIA.

2.3.2 Entry, descent and inflation

The launch dates are determined by the Earth-Mars launch windows and the dates of the summer solstices on Mars. The summer solstices do not always coincide with the arrival dates associated with Hohmann trajectories between Earth and Mars, so in many cases a non-optimum trajectory will have to be chosen. The low mass of the spacecraft permits departure and arrival at high C_3 with a relatively small launch vehicle, while also permitting early atmospheric deceleration with existing entry capsules.

As Hall et al. [17] showed, successful atmospheric inflation depends on the vehicle being able to decelerate to 25 m/s or less from an entry velocity of 7 km/s or higher, before it goes below 1 km from the surface. The low aerobot mass and the low elevation (–2 km MOLA) of the target destination provide large margins for entry and descent performance. For reference, a 2.65-metre capsule can land a maximum of 350 kg at –2 km [28]. This capsule diameter was used for Phoenix and Pathfinder.

A 17-metre supersonic parachute is assumed to slow down the package prior to inflation, trailing behind the package by at least 80 metres to avoid flagging motions and wake-induced parachute collapse. A pressurised bottle is attached to the bottom of the gondola, containing enough compressed hydrogen gas to fill the envelope. Previous work indicates that the needed amount of hydrogen can be stored in a 18 kg bottle at 525 bar, for an extended period of time without losses [29]. During the inflation phase, the hydrogen is valved into the tether and envelope at an increasing flow rate, to avoid ripping the envelope. The bottle is then dropped and the balloon left to reach its equilibrium altitude [17].

2.3.3 Timeline

The timeline is bookended by the crocus date, the date when the last of the CO_2 sublimates at a particular latitude, at the start and by declining sunlight at the end, though an extended mission might be possible, depending on how quickly the balloon travels to lower latitudes. Near the pole, the crocus date is Ls = 95° [18]. This date is after the summer solstice (Ls = 90°), when the solar flux is at its peak and the sun is above the horizon throughout the day. As the mission continues towards autumnal equinox at Ls = 180°, the minimum solar insolation will decline until the sun begins to dip below the horizon. At the earliest, HYPATIA can arrive after the summer solstice on August 25, 2021, but there are many other summer solstices to choose from [30].

In order to simulate the solar insolation at the northern PLD as a function of time, an implementation of the NASA Goddard Sunclock Algorithm [31] was prepared in MATLAB (Appendix A). It also took in account the optical depth of the atmosphere at low solar elevation. For the beginning of this simulation, a Julian date corresponding to August 25, 2021 was used.

The results showed that solar insolation varies on a vertical plane between 210 and 275 W/m^2 during the day at the summer solstice at 85° N. At 80° N, the date at when the sun crosses the horizon was found to be before January 1, 2022, with a maximum insolation of 260 W/m^2. The total duration for the mission is baselined at 90 sols, with an absolute maximum of 126 sols, without assuming significant progress to lower latitudes south of the margin of the NPLD.

This mission comes with a lengthy development and testing phase due to the lack of prior experience with balloons on Mars. Five years was allotted to the timeline for development before formal submission to the NASA Discovery program. Chapter 6 covers the future work to be done in order to validate the concept for flight on Mars.

2.3.4 Martian balloon flight

For propulsion, the aerobot relies upon the katabatic wind, which flows perpendicular to the spiral troughs in the NPLD [32]. On the average, the direction of this wind is constant from year to year, based on observed wind streaks, and provides a relatively predictable horizontal path for the aerobot until it crosses south of 80° N. The known wind streak directions are shown in Figure 1 from [32].

For the vertical component of the flight path, buoyancy control is achieved by venting gas. Knowing the atmospheric density and pressure with altitude starts with the scale height H (Equation 1), which is the vertical distance over which the atmospheric density and pressure fall off by a factor of 1/e:

$$H = \frac{kT}{\bar{m}g} \tag{1}$$

where k is the Boltzmann constant (1.38×10^{-23} J/K), T is the air temperature in Kelvins, $\bar{m}$ is the molecular weight of the atmosphere in kg, and g is the gravitational acceleration on Mars ($3.71\ \text{m/s}^2$). The molecular weight is found by dividing the atmospheric molar mass of 43.34 g/mol [33] by the number of molecules in each mole, also known as Avogadro's Number (Equation 2):

$$\bar{m} = \frac{43.34}{6.022 \times 10^{23}} \tag{2}$$

$$\bar{m} = 7.197 \times 10^{-23}\ \text{g}$$

$$\bar{m} = 7.197 \times 10^{-26}\ \text{kg}$$

At this atmospheric molecular weight and temperature of 205 K [34], the local scale height was calculated to be 10.6 km.

The mission would begin at the higher parts of the NPLD, at h = –2 km MOLA [22]. At this point, the atmospheric pressure P was estimated to be 737 Pa, based on the scale height H and datum pressure P_0 of 610 Pa, as shown in Equation 3:

$$P = P_0 e^{-\left(\frac{h}{H}\right)} \tag{3}$$

$$P = 610 e^{\left(\frac{2}{10.6}\right)} = 736.67\ \text{Pa}$$

At the NPLD rim at h = –4 km, the pressure increases to 890 Pa. To float near the ground at the increased atmospheric density, the vehicle will also need to slightly increase the density of its lifting envelope. This can be done in one of two ways – contracting the envelope or introducing small amounts of CO_2 into the envelope. A thorough analysis of these options is beyond the scope of this thesis.

The molecular weight $\bar{m}$ for hydrogen (molar mass = 2.00 g/mol), is 3.32×10^{-27} kg. Using the ideal gas law (Equation 4),

$$P = \left(\frac{\rho}{\bar{m}}\right) kT \tag{4}$$

which is a good approximation at ambient Martian conditions, the hydrogen density ρ_{H_2} at h = -2 km was found to be 8.65×10^{-4} kg/m^3. As an initial estimate, the bulk mass m_B of the balloon vehicle is found from the density of the gases and the volume of atmosphere V_B that the balloon displaces according to the static equilibrium between the buoyant force F_B and the balloon vehicle weight F_g (Equation 5):

$$F_B = F_g \tag{5}$$

where F_B comes from the difference in densities of the atmospheric and lifting gases, ρ_{CO_2} and ρ_{H_2}, respectively, multiplied by the balloon volume V_B and the gravitational acceleration g. F_g is just the vehicle mass m_B multiplied by the gravitational acceleration g:

$$(\rho_{CO_2} - \rho_{H_2})V_B g = m_B g \tag{6}$$

On both sides, the g term can be cancelled out, leading to:

$$(\rho_{CO_2} - \rho_{H_2})V_B = m_B \tag{7}$$

Equation 7 is then rearranged to illustrate the relationship between the vehicular density and the difference in the gas densities (Equation 8). ρ_{CO_2} comes from the known atmospheric density (NSSDC, 2015), corrected for –2 km altitude.

$$\frac{m_B}{V_B} = \rho_{CO_2} - \rho_{H_2} \tag{8}$$

A detailed estimate of the total balloon mass is given in Table 2.1 (Section 2.5.1). At 17 kg, the lifting gas volume is 739 m^3, using about 630 grams of hydrogen gas.

Landing is handled with a rubber ribbon trailing off the gondola that is dragged along the ice to slow the vehicle down to the point where the gondola makes contact with the surface. Lahayne et al [35] carried out experiments with rubber on ice, and obtained friction coefficients (μ) of up to 0.7 at temperatures as low as -13 degrees C. These friction coefficients varied, but were found to trend upward as the ice became colder and rougher. The braking distance d was estimated with Equation 9.

$$d = \frac{v^2}{2\mu g} \tag{9}$$

Using $\mu = 0.7$, $g = 3.71$ m/s^2, and $v = 12$ m/s, the braking distance was estimated to be about 28 metres.

2.3.5 Surface operations

As described in Section 2.5.7, the solar panels are mounted on the tether instead of the gondola. The envelope retains sufficient gas to remain aloft during surface operations. This has the added benefit of conserving lift gas and reducing the amount of water to be obtained at each site.

Water is procured from the ice with a short electrothermal drill that penetrates several centimetres into the ice. Water ice sublimates below the triple point, so handling of liquid and solids is not necessary. The mass of the electrothermal drill is baselined on the Planetary Volatiles Extractor from Honeybee Robotics [36], which masses 500 g.

When the electrothermal drill bites into the ice, an enclosed volume is created inside the gondola, allowing the partial pressure to increase as more water is sublimated, to the point where liquid water forms and trickles into the electrolysis stack. The water is then sent through a deionisation membrane and electrolysed into hydrogen and oxygen. The oxygen gas is vented while the hydrogen is sent up the tether and into the envelope, propelled by positive pressure from the electrolysis cell. An analysis of the needed partial pressures and power requirements is given in Section 2.5.3.

At takeoff, the ice-contacting surfaces are reheated to de-adhere from the ice. The force to release the aerobot is provided by the katabatic wind, with the balloon acting as a sail.

2.3.6 Communications scheme

The gondola is too small to mount a directional antenna, so all communications with the ground station takes place through a low-gain whip antenna (two for redundancy) with a sun-synchronous orbiter acting as a relay. Mars Reconnaissance Orbiter is in the right orbit for this purpose [37].

2.3.7 Planetary protection

HYPATIA does not carry instruments for the detection of extant life, but there is a possibility that the NPLD layers are home to detectable organic molecules. This is not enough to define a Special Region where there is a chance of discovering biological activity according to the guidelines set by the Committee on Space Research (COSPAR) [38]. HYPATIA would thus fall under the IVa category as defined by the NASA Office of Planetary Protection, necessitating the use of extensive documentation, bioassays, probability of contamination analysis, and an increased number of procedures [39]. The latter includes sterilization of the thermal drill.

2.4 Mission risks and mitigation strategies

2.4.1 Katabatic wind reliability

As a balloon aerobot, HYPATIA is dependent on the speed and direction of the polar katabatic winds. SHARAD radar altimetry of the polar surface has shown that the slopes of the spiral troughs generally do not exceed 15° from the horizontal on the downwind side and 1° on the upwind side [40]. Flow models of the troughs estimate the katabatic wind at 6 to 12 m/s at a flow height of 275 to 424 m [21]. Based on visible wind streaks, the katabatic winds are believed to only flow perpendicular to the troughs until they reach the NPLD rim [41].

When the gondola is on the ice, there is a risk of the balloon being blown further away from the gondola and closer to the surface at higher wind speeds, where it could adhere to the ice. Placing the gondola on only the equatorial-facing slopes mitigates this risk, since they are down the wind and steeper than the upwind, pole-facing slopes. The troughs are a few hundred meters deep, spaced a few kilometres apart, so this positioning is not expected to pose a risk.

Since the katabatic winds are driven by the presence of CO_2 ice and are reinforced by the thermal contrast across the crocus line, they disappear once the upwind CO_2 ice is gone. Once that happens, the winds are more subject to transient eddies and synoptic structure. This imposes another requirement on the mission to land somewhere where the CO_2 has already retreated but there is still some upwind CO_2 ice to drive the necessary winds, potentially driving the start date to some point before the northern summer solstice.

2.4.2 Terrain

The additional requirement to repeatedly land on the surface demands that the terrain be relatively flat to minimise hazards. The Context Camera on Mars Reconnaissance Orbiter found only 130 craters on the NPLD [42]. The HiRISE camera on the same orbiter failed to detect rocks at its resolution of 25 cm/pixel [43]. These two lines of evidence point towards a sparse distribution of rocks on the NPLD, with any existing rocks below 25 cm in size.

2.4.3 Layer surface weathering

The layers of the NPLD are exposed on the leeward (equator-facing) slopes of each trough due to katabatic winds. The same winds play a role in eroding the slopes so they gradually move northward, with the stoss (pole-facing) slopes following suit as the katabatic wind deposits leeward-slope material on them. This causes the leeward slopes to be significantly darker than the surrounding ice, due to dust-rich layers with low albedo. However, radar-return evidence from the SHARAD instrument shows that each dark layer is only 5% dust [44].

2.5 Aerobot

2.5.1 Driving requirements

The aerobot has several mission requirements that drive its design. At the highest level, it shall have the ability to:

1. survive a cruise of up to ten months (imposed on all subsystems and partially the responsibility of the cruise stage)

2. survive entry into the Martian atmosphere

3. deploy its balloon without tangling the lines or ripping the envelope material

4. hold hydrogen gas inside its envelope during flight and provide a suitable environment for liquid water inside the same envelope during surface operations

5. keep the balloon inflated and aloft while the gondola is on the ice

6. communicate with Earth via an orbiting relay at low data rates

7. detect terrain during flight and make decisions about when to land independently of the ground control team

8. grip the ice and secure itself for melting and electrolysis

9. image the terrain in the visible and infrared spectra, and take atmospheric readings

10. sublimate ice and analyse the vapour with an instrument sensitive to different isotopologues of water.

The data rate in requirement 6 depends on the size and resolution of the images taken with the nadir imager (Section 2.5.4). The spectrometer has a much lower data rate and is used while the imager is dormant, so it does not dominate the communication requirements.

The potential design of a balloon envelope satisfying requirements 3–5 is presented in Sections 2.5.2–2.5.3. The design of a gondola satisfying requirements 6–10 is provided in Sections 2.5.4–2.5.9. The subsystems of the aerobot are summarised in Table 2.1.

Table 2.1: Mass and Power Allocations of the Aerobot

Subsystem	*Mass (g)*	*Volume (cm³)*	*Peak power (W)*	*Energy (W-hr)*
Avionics (2)[1]	1,098	320	10.8	259.2
Science[2]	1,476	1,187.32	7.57	44.8
Communications[3]	70	10	3	18 (at 3 W) 1.8 (at 300 mW) 0.6 (at 100 mW) 0.3 (at 50 mW)
WEC Stack[4]	300	253	5	5
ET Drill[5]	500	262.19	7	7
Tether	1,440	600	N/A	N/A
Anchor Ribbon	190	200	5	0.002
Thermal control	500	500	5	120
Power	4,039	6,505.4	N/A	N/A
Gondola Structure	1,300	465	N/A	N/A
Gas Envelope	3,600	N/A (much larger than gondola)	N/A	N/A
MARGIN (15%)	2176.95	1545.4365	6.5055	68.1003
TOTAL	16689.95	11848.3465	49.8755	522.1023

Notes: [1] RAD750 3U [45]
[2] Table 2
[3] Assuming 25% duty cycle (15-minute orbital passes once every hour)
[4] Tethers Unlimited HYDROS custom electrolysis cell [46]
[5] Based on Honeybee Robotics Planetary Volatiles Extractor [36]

2.5.2 Gas envelope

The prospective envelope design is a sphere. Mylar was chosen for the envelope material for its high elastic modulus, ability to support a metallic coating and ability to withstand temperatures down to 203 K without degradation. It has a density of 1.39 g/cm^3 [47]. Gas is released through a lightweight radio-controlled top vent developed at JPL [48]. With a 1/4-mil sheet of Mylar (areal density of 8.9 g/m^2) and a 100-nm aluminium coating (0.3 g/m^2), an 11-m diameter envelope masses 3.6 kg. A metallised coating was assumed in order to reduce gas permeability and ultraviolet exposure.

2.5.3 Lifting gas procurement

The viability of this mission depends on the ability to maintain water as a liquid inside the gondola despite ambient conditions. This is due to the present state of the art of water electrolysis. A custom electrolysis cell has been tested at Tethers Unlimited and requires its feedstock to be pure deionised liquid water [46]. It measures 85 by 85 by 35 mm and uses 5 W of power.

Since the balloon remains inflated at all times, with descent controlled by small leakages of gas, only a small amount of hydrogen needs to be replenished at each site. For a baseline amount of 1 gram, 9 grams of water must be mined. At the extremely low partial pressures on Mars, water ice undergoes sublimation instead of melting. Assuming an enthalpy of sublimation of 51 kJ/mol [48], it takes 25.5 kJ to sublimate 9 grams of ice. Losses due to heat conduction in the surrounding ice will increase this figure, but the efficiency of this process can be maximised by using pulses of intense heat to quickly sublimate the ice before the heat is conducted away. This energy can be delivered at 7 W-hr for one hour, or less at longer drilling times.

A condensation cavity just above the drill and spectrometer, insulated and maintained at above 273 K during the water procurement periods, allows the vapour to gather and self-pressurise when the drill is in the ice. The limited enclosed volume ensures that the partial pressure quickly surpasses the triple point with a few moles of water.

The abovementioned electrolysis cell provides 10.5 cubic centimetres per minute of H_2 at 5 W, enough to supply 1 gram in 5 microseconds. It is at TRL 5-6, so a flight-qualified unit can be prepared in time for a 2020 launch.

2.5.4 Tether

The tether serves several purposes. Firstly, it holds the envelope and gondola together. Secondly, it is a conduit for hydrogen gas to travel up into the envelope. Finally, it supports the suspended solar panels and lightweight instruments along its length and distributes power between them and the gondola. A possible design is shown in Figure 2.2, with the gas conduit inside the tether.

Figure 2.2 Cross-sectional and lengthwise views of tether

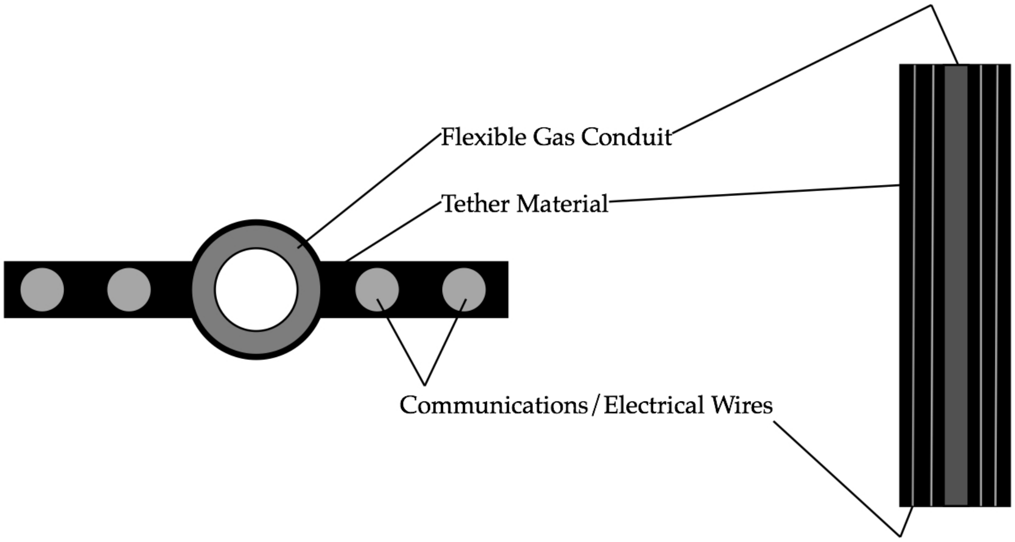

Parallel aluminium wires were assumed for redundancy and to minimise resistance losses, but even with a single thin wire, the resistance was found to be negligible. Dyneema was chosen as the tether material for its light weight and high tensile strength, minimising the amount of material used [49]. At a density of 0.975 g/cm^3, a width of 4 cm, and a thickness of 0.18 cm, a 20-metre tether weighs about 1,440 g.

The work-energy principle (Equations 10 and 11) was used to quantify the shock load on the tether during deployment:

$$Fd = \frac{1}{2}mv_f^2 - \frac{1}{2}mv_i^2 \qquad (10)$$

$$F = \frac{m(v_f^2 - v_i^2)}{2d} \qquad (11)$$

where m is the mass being decelerated in kg, v_i and v_f are the initial and final velocities in m/s, d is the deceleration distance in meters, and F is the shock force in Newtons.

From the JPL spherical stratospheric balloon deployment tests [17], v_i was assumed to be 25 m/s, v_f was assumed to be 30 m/s, and d was assumed to be 500 m. The mass to be decelerated was assumed to be the entire vehicle (Section 2.5.1, Table 2.1) plus the hydrogen bottle (Section 2.3.2), for a total of 36 kg. F thus works out to be 9.9 N.

The deployment stress σ in Pa depends on the cross-section area A of the tether. Letting it be 4 cm wide and 0.18 cm thick ($A = 7.2 \times 10^{-5}$ m^2), the resulting stress is:

$$\sigma = \frac{F}{A} \qquad (12)$$

$$\sigma = 137{,}500 \text{ Pa}$$

Dyneema has a tensile strength of 3.4 GPa [48]. The safety factor of this tether is the maximum stress σ_{max} it can support divided by the stress σ_{load} it is holding (Equation 13).

$$SF = \frac{\sigma_{max}}{\sigma_{load}} \tag{13}$$

In this scenario, the safety factor is 24,727.3. Under the expected descent and inflation conditions, tether breakage is not considered to be a risk.

2.5.5 Scientific instruments

Several potential instruments may be considered for placement on the gondola and tether, based on existing and near-term hardware. They are given in Table 2.2. The air temperature and wind velocity sensors are of low mass and particularly sensitive to heating from the gondola. They are placed on the tether to avoid any heat sources and air-flow interference from the gondola. Multiple sensors along the tether establish a temperature and velocity profile with height.

Table 2.2: Payload Instruments

Payload	*Mass (g)*	*Volume (cm³)*	*Idle/Peak Power (W)*	*Energy (W-hr)*
Air Temperature Sensor (2)[1]	30	2	0/0.02	0.48
Wind Velocity Sensor[2]	30	2	0/0.02	0.48
Pressure Sensor[3]	35	53.04	0/0.015	0.036
Relative Humidity Sensor[4]	15	40	0/0.015	0.036
Ground Temperature Sensor[5]	20	21.28	0/0.00025	0.0006
Tunable Laser Spectrometer[6]	1,000	700	0/0.75	1.8
Nadir Imager w/ Optics[7]	346	369	1.75/2.5	42
TOTAL	1,476	1,187.32	1.75/3.3	44.8326

Notes: Specifications given are minimum achievable based on:

[1] air temperature sensors [50]

[2] anemometers (comparable technology to air temperature sensors)

[3] MSL pressure sensor [51]

[4] MSL REMS humidity sensor [51]
[5] MSL REMS ground temperature sensor [51]
[6] [52]
[7] MSSS ECAM-C50 with wide-angle optics [53],[54]

The data sampling strategy to be used is similar to that in a micro weather station proposal [50]. The air temperature and wind velocity would be sampled at 1 Hz because of their importance to the continued function of the balloon, with the other qualities being sampled less frequently. For the energy column in Table 2, the duty cycles for the TLS, pressure, humidity, and ground temperature sensors was assumed to be 10%. The energy figure for the imager used a 100% duty cycle at idle power, under the assumption that this instrument would only reach its peak power when commanded to.

Tunable laser spectrometry (TLS) can be resolution-tuned to specific species in a sample, and offers non-destructive analysis unlike mass spectrometry. It would be primarily used to detect deuterium/hydrogen ratios in water (in the form of HDO/H_2O). Based on SAM-TLS, HDO at natural environmental levels on Mars corresponds to a 3–7% signal and needs resolution of better than 0.025 cm^{-1} at 3,594 cm^{-1}. Recent advances in TLS suggest a 1-kg device consuming 750 mW of power [52].

5.6 Gondola structure

The gondola structure is determined by several requirements:

- maintain the operational and structural integrity of the payload during flight
- protect the payload from impacts at 12 m/s
- keep the gondola upright during surface operations at low slope grades
- withstand parachute and balloon opening shocks
- hold and release the hydrogen inflation bottle during and after EDI
- take up no more than 25% of the payload mass.

These requirements can be fulfilled with an aluminium isogrid and carbon fibre bridle. Hollow aluminium tubes are provided for the support members and skids, to save mass and to protect major electrical wires. A prospective design is shown in Figure 2.3.

Figure 2.3: Prospective design and location for gondola (with instruments) (see online version for colours)

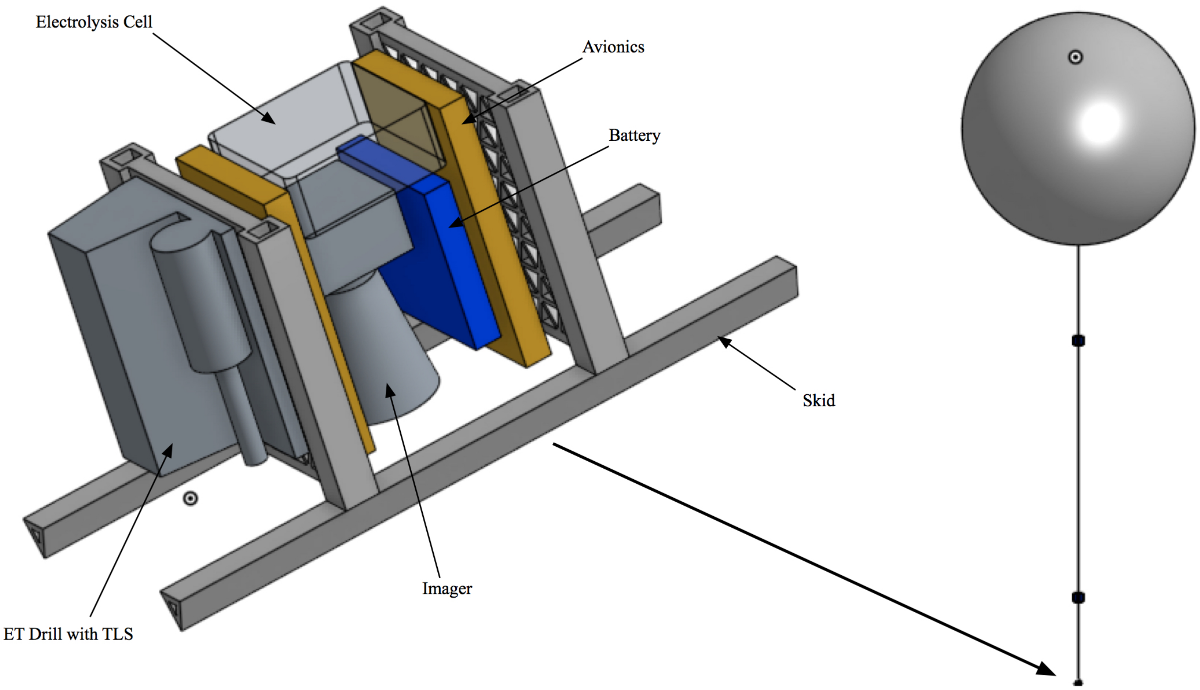

As modeled, the gondola is 37 cm long, 16 cm wide, and 17 cm tall (not including the carbon fibre bridle which would connect it to the tether). With aluminum-6061 construction, the structure masses approximately 1,300 g.

2.5.7 Power subsystem

At local summer at 80–90° N, the sun is no higher than 25° from the horizon and will appear to revolve 360 degrees around the sky over a sol. This, in addition to winds, mandates the use of omnidirectional solar panels instead of lighter tracking arrays.

The solar panels are mounted on the tether. Tether mounting allows more solar panels to be added and there is no risk of obstruction or damage due to terrain. This frees up the gondola for optimisation in other directions. As modelled, an aluminium frame can mass 928 g for six solar panels arranged in an outward hexagonal pattern (Figure 2.4). Each panel has 970.5 cm^2 of area. Assuming 1.76 kg m^{-2} for triple-junction panels [55], the total solar panel mass is 1,024.8 grams on one frame. This setup is capable of outputting 10 W in 210 W/m^2 of illumination at 28% efficiency, regardless of solar azimuth. Two solar arrays were baselined to provide margin, at a total mass of 3.9 kg.

Figure 2.4: Prospective design and locations for tether-mounted solar panel arrays (see online version for colours)

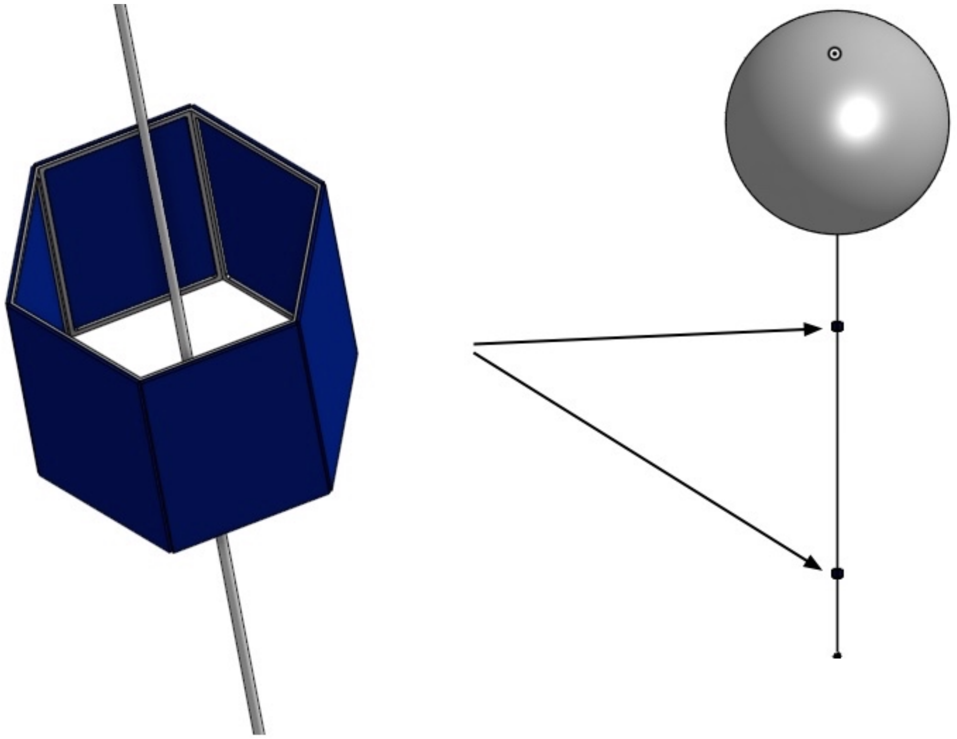

Two of the solar arrays described above can provide 20 W at minimum. To provide for unexpected blackouts and higher power usages, a 20 W-hr lithium polymer battery (~150 W-hr/

kg) was chosen for at least the computers and a few other functions. The battery mass is 133 g [56].

2.5.8 *Thermal control subsystem*

The thermal control subsystem must keep the temperature-sensitive payload within their operating temperatures, with radiative heating of 200 W/m^2 or above from the sun and convective cooling from the katabatic wind at the ambient atmospheric temperature of around 205 K. The solar panels and tether instruments are physically separate from the gondola and do not need to be heated. The antennas are on the gondola but do not require heating.

In particular, the avionics, imager electronics, and spectrometer need to be kept above 243 K and the electrolysis cell above 273 K (Table 2.3). A warm electronics box consisting of several layers of Mylar with vacuum-deposited gold is sufficient to keep these instruments and the flight computer within their operating temperatures, with the possible addition of electric heaters.

Table 2.3: Temperature Ranges of Spacecraft Components (HYPATIA)

Component	*Allowable Flight Temperatures (K)*	
	Operational	*Survival*
CPU	258 to 318	243 to 333
Solar Panels	123 to 383	73 to 403
Antennas	173 to 373	153 to 393
Nadir Imager*	243 to 313	-
Spectrometer	Unknown (assumed similar to imager)	-
WEC**	>273	-
Condensation Cavity**	>273	-

Notes: * [53], [54]
**Needs liquid water to function
Sources: [57], p.428, [58], p.348

The bulk temperature of the gondola was estimated by summing all the internal, solar, planetary infrared, and planetary albedo fluxes and balancing it with the spacecraft radiation temperature in Equation 14. S is the solar flux at 210 W/m^2. A_x and A_s are the cross-sectional and surface areas of the gondola, respectively. T_{Mars} is the temperature at the local surface (205 K). α and ϵ are the absorptivity and emissivity of the outer gondola surface, respectively. The albedo of ice (0.7) was used in this estimate.

$$\text{internal heat dissipation} + S\alpha A_x + (\epsilon\sigma A_x T_{Mars}^4) + (S\alpha A_x)(\text{albedo}) = \sigma\epsilon A_s T^4 \qquad (14)$$

With an internal heat dissipation of 5 W and gold-coated Mylar with α = 0.19 and ϵ = 0.06, the gondola bulk temperature T was estimated to be 317 K (43 C).

This analysis leaves out the factors of wind convection and heat conduction. With atmospheric pressure so low on Mars, heat convection due to wind does not present much of an effect compared to heat conduction out of the bottom of the gondola into the ice. A more complete thermal model of surface operations is left up to future researchers.

2.5.9 Communication, control, command, and data handling

For a Mars balloon mission, the mass and data rates of the communications hardware are severely restricted. The descent imager, at 5 megapixels per image, will dominate communications and data handling requirements. Micro-transceivers have been introduced that mass less than 50 g, measure 10 cm^3, and consume less than 1 W of power [59]. They are cold- and radiation-tolerant, allowing them to be placed outside warm-electronics boxes and shielding.

At polar latitudes, overpasses by the Mars Reconnaissance Orbiter are frequent but low in the sky [37]. For this particular micro-transceiver, commands can be received at 2 or 8 kbps and science data transmitted at 100 kbps at 1 W, as long as the orbiter is high in the sky. At this rate, a 20-Mb photograph from the nadir imager can be transmitted in 3.3 minutes, assuming a typical compression of 4 bits per pixel (subframing each photograph down to 1024 by 1024 pixels would reduce the file size to 4 Mb). The more likely data rates are lower at higher slant angles.

2 Gb of flash memory is sufficient to hold 100 20-Mb images with no power consumption. The MSL RAD750-3U board [45] with the above modification is baselined for the avionics suite, with two units for redundancy.

2.6 Discussion

As discussed in the previous sections, a hopping balloon vehicle has the potential to efficiently explore the exposed ice layers in the NPLD spiral troughs in one launch and at very low mass. The low mass of the proposed vehicle opens up the possibility of sending several similar vehicles to the NPLD in one launch, each in their own atmospheric entry capsule. While each aerobot takes up very little of the internal volume of a 2.65-metre capsule, packing more than one aerobot inside a single capsule is inadvisable due to EDI complications (such as the risk of parachute lines tangling). Smaller heat-shield diameters may reduce the volume that each capsule takes up inside the fairing of the launch vehicle, at the cost of increased ballistic coefficients. A multiple-aerobot strategy, besides providing redundancy, would enable a more complete exploration of the NPLD along several routes with the local katabatic winds.

3: Saturn Ice Ring Exploration Network (SIREN)

3.1 Overview

One appealing niche for small spacecraft is the exploration of the rings of Saturn. In light of the 2013-2022 Planetary Science Decadal Survey, which notes on page 190 that “Nearly all constituent ring particles are too small to observe individually, even from an orbiting spacecraft, so a proper interpretation of any observations requires an understanding of the particles’ collective effects and behavior,” [60], there is a need for close-up imaging and sampling of the Saturnian rings to answer questions about their composition, dynamics, and evolution. Direct sampling of ring particles will necessarily involve at least one low-speed, controlled collision.

Contact science on the individual ring particles is impractical with a large spacecraft, due to the short mean free path between collisions [61]. This environment is more conducive to a few small spacecraft, sized at the CubeSat form factor or larger, that can provide the Δv needed to approach the ring plane and avoid collisions. There is still a need for a mothership capable of the larger Δvs needed for a hover-orbit above the ring plane and to traverse the rings to another orbital radius so the daughtercraft can be reused at the next location as well as for relaying communications back to Earth. The energies associated with orbital insertion and changes preclude the daughtercraft from executing these tasks on their own.

A mission similar to the mothership described above is already listed in the Decadal Survey. Page 189 of this document states that “In future decades, a dedicated Saturn Ring Observer mission could potentially obtain in situ Saturn ring data with unprecedented spatial resolution and temporal coverage. Initial engineering studies for such a mission exist, but further technology development is required during the next decade to develop a robust mission profile” [60].

This chapter will present a potential mission concept to advance Saturn ring science using a few small daughtercraft deployed from a mothership similar to the Saturn Ring Observer (Spilker et al, 2010). The daughtercraft are small enough to venture into the rings to take scientific measurements that would be impractical with a larger spacecraft. Each one is optimized for a specific task, from ice particle sampling to ion and neutral particle measurements. The mothership provides recharging, downlinking to Earth, and transportation between different orbital radii. This mission is designated Saturn Ice Ring Exploration Network (SIREN). As described, SIREN is not a complete system or payload design, but rather a platform for contact science in the rings for which new instruments and technologies could be developed.

3.2 Close-in study of the rings

3.2.1 The scientific value of the Saturnian rings

The 2013-2022 Planetary Science Decadal Survey lists the origin and long-term evolution of the Saturnian rings as one of the major unsolved problems in planetary science, with contact science as one of the priorities of future missions [60]. On Page 79 of the document, the need to study planetary ring systems is justified: "Exploring the rings of Saturn, Uranus, and Neptune is of high scientific priority, not only to deepen understanding of these giant planet systems but also to obtain new insight into exoplanet processes and their formation in circumstellar disks, albeit of enormously different scale".

The rings of Saturn are the most extensive planetary rings in the solar system, the densest part of which (designated as the A, B, and C rings) stretches from 14,230 to 76,510 km in altitude above the 1-Bar level of the Saturnian atmosphere (orbital radii between 74,500 and 136,780 km) and consisting of >99% water ice with impurities that strongly absorb ultraviolet [62]. It is not yet known whether the rings originated from the tidal disruption of an ice-mantled moon, multiple cometary captures and breakups, or something else. As with terrestrial ice cores, inclusions trapped in the ice particles may give clues to the history of the rings that constrain our current models of planetary ring evolution [63].

3.2.2 In-situ sampling of the ring particles

To date, no spacecraft has directly sampled the Saturnian rings. The composition of the rings has been constrained by their reflection spectra, but in-situ sample gathering and analysis would put to rest several questions about their formation and evolution. For instance, the pristine appearance of the main rings is inconsistent with meteorite infall, which would have resulted in significant darkening over Ma-timescales [64]. It is also inconsistent with their apparent mass, which implies the breakup of an ice moon or many cometary disruptions within the Roche limit, both of which are unlikely within the last 10^9 years [65]. A possible resolution to this paradox is recycling of material to keep the rings youthful-looking despite their age, but the precise mechanism has not been established [61].

The Decadal Survey also mentions the possibility of dust entrained in the ice on page 193. "Near-infrared spectral studies of the Galilean and saturnian moons and rings have led to new models for dust contamination of icy surfaces, but definitive identification of the chemical species involved remains elusive and may require in situ sampling" [60].

3.2.3 Measurements of the ring environment and particle dynamics

The ability to sample the ring particles also brings with it the ability to directly measure quantities in the general ring environment, such as its gas distribution [66]. Cassini measured this variable remotely, but it is not yet known how they interact with the particles in the A, B and C rings.

There is also a lack of close-up knowledge of ring particle dynamics in the azimuthal, radial, and height directions. The Saturn Ring Observer mission proposal called for a medium-class spacecraft in a "hover" orbit a few kilometers above the ring plane, studying the particle dynamics at 0.45 cm/pixel resolution [67]. This mission concept would use a scanning laser altimeter that could infer, and possibly measure directly, the z component of particle velocities. It could be improved by adding a few secondary smallsats to provide images in close succession from inside the ring plane, making direct velocity measurements in the z direction possible. From there, improved coefficients of restitution can be made from the collisions between particles. Direct observation of the ring particles, including their size distribution, would also help deduce the physics of accretion in a strong tidal field and in turn constrain the age of the rings [68].

3.2.4 Science Objectives and Requirements

The science objectives and requirements of each SIREN daughtercraft are outlined below. The general objectives are:

O1 Determine the size and distribution of particles in the A, B, and/or C rings (can be descoped to one ring depending on the propulsion system available to the mothership)
O2 Determine the minimum, maximum, and average number and mass densities of the A, B, and/or C rings
O3 Determine the relative velocities of the ring particles and their coefficients of restitution
O4 Determine the morphology of the large (>1 m) ring particles
O5 Quantify the chemical composition of the impurities in the ring particles
O6 Quantify the chemical composition and distribution of the ion and neutral particle environment in the rings
O7 Quantify the magnetic field vectors and magnitudes in the vicinity of the rings
O8 Determine if the larger ring particles have a significant component of materials other than water ice

The requirements to fulfill these objectives are as follows:

R1 A visible-light camera capable of 10 cm/pixel at 800 meters (fulfills O1 through O4)
R2 An alpha-particle X-ray spectrometer for contact science, capable of finding the abundance/distribution of trace elements and compounds in the ice (fulfills O5)
R3 An ion and neutral mass spectrometer sized for CubeSats (fulfills O6)

R4 A CubeSat-deployable magnetometer capable of readings in the 21-microTesla range (fulfills O7)

R5 A thermal auger that can burrow into a >1m ring particle and remove a cylindrical sample for delivery to the mothership for further analysis (fulfills O8)

3.3 Mission Profile

3.3.1 Concept

The mission profile concept is shown in Figure 3.1. After Saturn Orbit Insertion (SOI) and other corrections to lower the orbit, the mothership ends up just outside the outermost F Ring (Figure 3.1, Panel 1).

Figure 3.1: SIREN Mission Profile (see online version for colors)

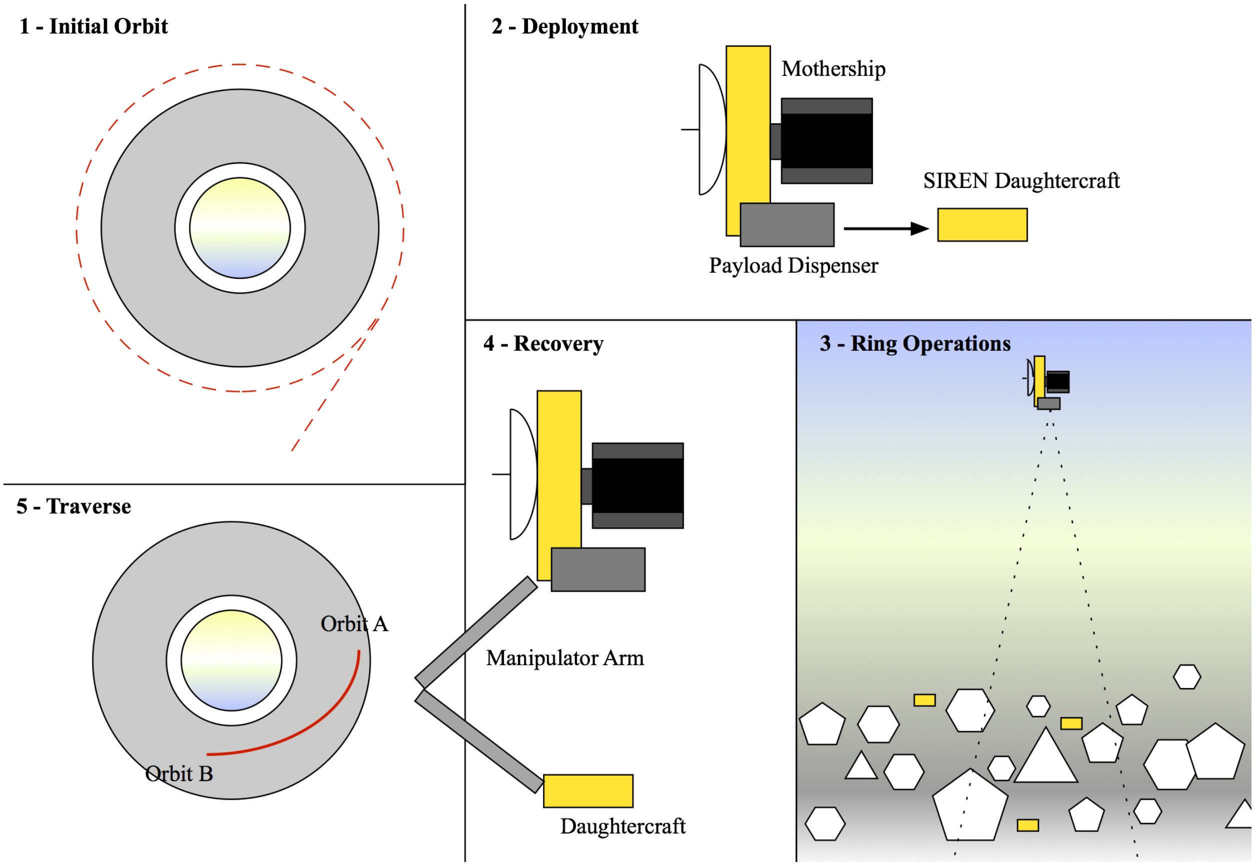

Notes: Beginning at the initial orbit (Panel 1), the mothership spirals down to its desired orbit and deploys daughtercraft (Panel 2) prior to imaging the ring plane (3). The daughtercraft are used to study the ring at low proximity, and are retrieved at the end of operations in this orbit (4) before the mothership traverses to another orbit closer to Saturn (5).

At this point, the mothership transitions to a “hover” orbit, with periods of thrusting perpendicular to the ring plane that advances the argument of periapsis of its orbit so it stays a few kilometers out of the ring plane. After this, the mothership begins its primary operations, including deploying daughtercraft (Panel 2). The daughtercraft execute an inclination change maneuver in the ring plane and analyze the ring environment and particles up close while the mothership takes images of the ring plane to quantify the relative velocities and coefficients of restitution of the particles (Panel 3). After operations are complete at this orbital radius, the daughtercraft are recovered (Panel 4) and the mothership traverses the rings to a shorter orbital radius, where it repeats the sequence (Panel 5). The A, B, and C rings are each examined in a similar way.

3.3.2 Ring operations

The orbit selection for ring operations is dictated by the requirement to track the ring particles at low relative velocities. This implies a low-inclination circular orbit near the ring plane that can only be reached from the high-eccentricity capture orbit at a Δv of ~16 km/s. The transition from the capture orbit to the initial circular orbit is too energetic for daughtercraft and instead we assume that the entire system performs this maneuver as described in the original Saturn Ring Observer concept [67].

There are at least three daughtercraft, each optimized for a different purpose. The first one, SIREN-A, approaches the ice particles in the ring plane to assist the mothership in quantifying the collision velocities and coefficients of restitution of the ring particles, by providing relative velocities in the ring-height (z) direction. These tasks can be carried out with imagers at visible, wavelengths.

The second daughtercraft, SIREN-B, carries an ion and neutral mass spectrometer to map the ionized particle environment. In addition, it includes field sensors to quantify the magnetic fields and gradients in the ring plane.

Finally, the third daughtercraft (SIREN-C) carries an imager with variable focal length for close-up imaging of a specific ring particle of >1 meter diameter. The same daughtercraft also carries a thermal auger instrument to sample the ring particle. The daughtercraft are separate because putting all their instruments on a single spacecraft would make it too massive to easily avoid the ring particles.

Starting from the outer A ring (at an orbital radius of 139,000 km or below), the daughtercraft are deployed from the mothership by the use of dispensers similar to the proposed Canisterized Satellite Dispenser [69]. They would be on a slightly inclined orbit that carries them into the ring plane. SIRENs A, B, and C would execute an inclination-change maneuver after arriving at the ring plane. All three daughtercraft uplink their data to the mothership via crosslinks between low-gain antennas. These operations are constrained by the availability of stored energy on the daughtercraft and the duty cycle of each instrument and propulsion system.

Upon return, the daughtercraft are retrieved by the use of magnetically selective docking ports that guide the craft back into its dispenser, which has been spring-loaded for the next deployment.

3.3.3 Timeline

The pump-down design in Nicholson et al [67], stated as an operationally challenging one due to techniques invoked to reduce the pumpdown duration, nonetheless has a 3-4 year time period between Saturn arrival and start of the science mission. To accommodate the pump down period, the integrated craft would arrive at Saturn 3-4 years before the solstices, when the beta angle between the ring plane and the solar vector is at its highest. This maximizes illumination of the rings, and minimizes the time spent in eclipse.

Being the outermost of the main rings, the F ring would be the first to be reached from the initial capture orbit. In order of decreasing orbital radius, the A-ring, the Cassini Division, and the B-ring can be reached with sufficient time and/or propellant expenditure. The mission can end in one of two ways depending on its propulsion system: 1) when the daughtercraft run out of propellant or 2) when the mothership reaches the innermost edge of the C ring, with a possible extension to the D ring. Disposal would be accomplished by a final burn to send all spacecraft into the Saturnian atmosphere, as for the Cassini-Huygens mission.

3.3.4 Planetary protection

SIREN is not meant to land on a spherical planetary body containing liquid water, so its planetary protection requirements are considerably less stringent than for HYPATIA. Its mission objectives and profile place it within Category II of the NASA Office of Planetary Protection guidelines [39]. Simple documentation of a short planetary protection plan is required, including contingencies for inadvertent impacts.

3.4 Analysis and Trade Studies

3.4.1 Transfer & rendezvous between inclined circular orbits

Upon departure from the mothership, the SIREN-A, -B, and -C daughtercraft would already be on an inclined orbit that carries them into the ring plane. A simple plane-change maneuver, Δv_δ, without a radial velocity change or apse line rotation, would take place inside the ring plane and is described with Equation 15 [70]:

$$\Delta v_\delta = 2v\sin\frac{\delta}{2} \qquad (15)$$

where δ is the change in inclination (in radians) and v is the orbital velocity (in km/s). For orbital inclinations corresponding to a maximum offset of 2 km above the ring plane, the plane change Δv is 9.18×10^{-5} to 3.64×10^{-5} km/s (9.18 to 3.64 cm/s) for orbital radii between

74,000 and 137,000 km, respectively. This range of radii brackets the inner edge of the C ring and the outer edge of the A ring.

Returning to the mothership takes more than a plane change. The simplest case is a two-impulse rendezvous, assuming that both spacecraft have the same orbital parameters except for inclination (Table 3.1). The following steps from Equations 16 to 38 do not show the entirety of the algorithm, but the complete algorithm can be found in Appendix B.

Table 3.1: Example mothership and daughtercraft orbital parameters, in km and degrees

Orbital Parameter	Mothership	Daughtercraft
Semi-major axis (a)	137,000	137,000
Eccentricity (e)	0.0001	0.0001
Inclination (i)	1.2547E-04	0
Right Ascension (Ω)	20	20
Argument of Periapsis (ω)	0	0
True Anomaly (θ)	60	60

From these parameters, the state vectors of the spacecraft in the perifocal (orbit focus-centered) frame $\mathbf{r}_{\bar{x}}$ and $\mathbf{v}_{\bar{x}}$ can be converted into the state vectors in the Saturn-centric equatorial frame. The following assumes a maximum offset of 300 m from the ring plane to minimize Δv.

The state vectors of the mothership ($\mathbf{r}_0$, $\mathbf{v}_0$) and a daughtercraft ($\mathbf{r}$, $\mathbf{v}$) in the Saturn-centric equatorial frame at this instant are:

$$\mathbf{r_0} = (23{,}789.8\hat{\mathbf{i}} + 134{,}918.7\hat{\mathbf{j}} + 0.2598\hat{\mathbf{k}})\ \text{km} \tag{16}$$

$$\mathbf{v_0} = (-16.3866\hat{\mathbf{i}} + 2.8894\hat{\mathbf{j}} + 1.8218 \times 10^{-5}\hat{\mathbf{k}})\ \text{km/s} \tag{17}$$

$$\mathbf{r} = (23{,}789.8\hat{\mathbf{i}} + 134{,}918.7\hat{\mathbf{j}} + 0\hat{\mathbf{k}})\ \text{km} \tag{18}$$

$$\mathbf{v} = (-16.3866\hat{\mathbf{i}} + 2.8894\hat{\mathbf{j}} + 0\hat{\mathbf{k}})\ \text{km/s} \tag{19}$$

Figure 3.2 visually represents the two spacecraft, target A and chaser B, at the start of the maneuver in their frames of reference:

Figure 3.2: Frames of reference of target A and chaser B

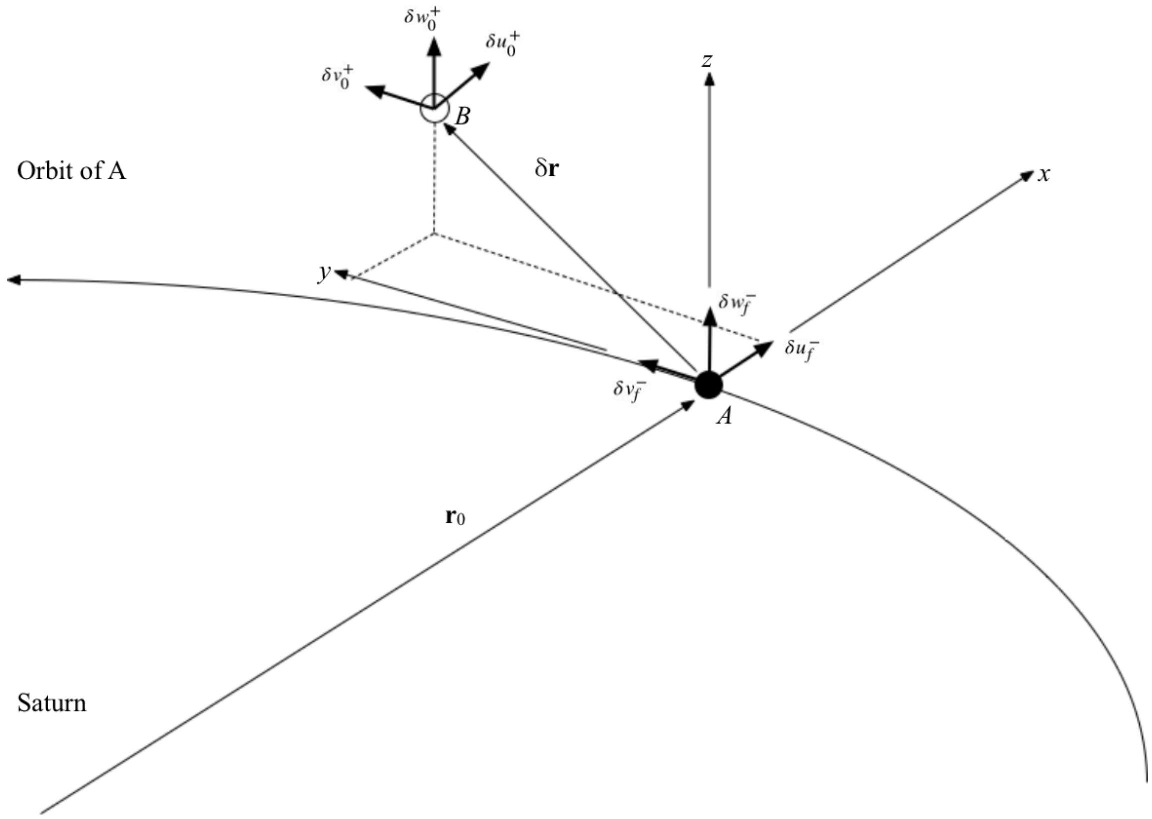

where δu_0^+, δv_0^+, and δw_0^+ are the components of the initial burn vector, and δu_f^-, δv_f^-, and δw_f^- are these of the final burn vector.

From Equations 16 and 17, the mothership reference frame unit vectors at this instant can be extracted by having the $\hat{\mathbf{i}}$ unit vector be the normalized position vector, the $\hat{\mathbf{j}}$ unit vector the normalized velocity vector, and $\hat{\mathbf{k}}$ the cross product of $\hat{\mathbf{i}}$ and $\hat{\mathbf{j}}$:

$$\hat{\mathbf{i}} = \frac{\mathbf{r}_0}{\|\mathbf{r}_0\|} = 0.1736\hat{\mathbf{I}} + 0.9848\hat{\mathbf{J}} + 1.8964 \times 10^{-6}\hat{\mathbf{K}} \tag{20}$$

$$\hat{\mathbf{j}} = \frac{\mathbf{v}_0}{\|\mathbf{v}_0\|} = -\,0.9848\hat{\mathbf{I}} + 0.1736\hat{\mathbf{J}} + 1.0949 \times 10^{-6}\hat{\mathbf{K}} \tag{21}$$

$$\hat{\mathbf{k}} = \hat{\mathbf{i}} \times \hat{\mathbf{j}} = 7.4895 \times 10^{-7}\hat{\mathbf{I}} + -2.0577 \times 10^{-6}\hat{\mathbf{J}} + 1.0000\hat{\mathbf{K}} \tag{22}$$

The $\hat{\mathbf{i}}$, $\hat{\mathbf{j}}$, and $\hat{\mathbf{k}}$ unit vectors make up the transformation matrix $[Q]_{Xx}$ from the Saturn-centric equatorial frame into the mothership frame:

$$[Q]_{Xx} = \begin{bmatrix} 0.1736 & 0.9848 & 1.8964 \times 10^{-6} \\ -0.9848 & 0.1736 & 1.0949 \times 10^{-6} \\ 7.4895 \times 10^{-7} & -2.0577 \times 10^{-6} & 1.0000 \end{bmatrix} \tag{23}$$

Each element in this matrix (Equation 23) is a direction cosine of each of the xyz axes in the accelerating local vertical, local horizon (LVLH) frame (target A in Figure 3.2) with respect to the Saturn-centric inertial frame axes. The position vector $\delta\mathbf{r}$ of the daughtercraft relative to the mothership in the Saturn-centric equatorial frame is at this instant:

$$\delta\mathbf{r} = \mathbf{r} - \mathbf{r}_0 \tag{24}$$

The relative velocity $\delta\mathbf{v}$ is given by

$$\delta\mathbf{v} = \mathbf{v} - \mathbf{v}_0 - \Omega_{mothership} \times \delta\mathbf{r} \tag{25}$$

where $\Omega_{mothership} = n\hat{\mathbf{k}}$ and n, the mean motion of the mothership, is

$$n = \frac{v_0}{r_0} = \frac{16.6394}{137{,}000} = 1.2146 \times 10^{-4} \text{ rad/s} \tag{26}$$

In mothership coordinates, the relative position vector (δr_0) at the beginning of the rendezvous maneuver is given by

$$(\delta \mathrm{r}_0) = [Q]_{Xx}(\delta \mathrm{r}) \tag{27}$$

The relative velocity just before launch into the rendezvous trajectory (δv_0^-) is given by

$$(\delta \mathrm{v}_0^-) = [Q]_{Xx}(\delta \mathrm{v}) \tag{28}$$

The orbital period T is almost 6 hours at the 74,000-km radius, and increases with radius (Equation 29 where the gravitational parameter μ is 37,931,000 km^3/s^2).

$$T = \frac{2\pi}{\sqrt{\mu}} r^{\frac{3}{2}} \tag{29}$$

Each orbit intersects the ring plane at two points, so at least 2 hours was allocated for the return leg to avoid complications from the ring plane during rendezvous. The Clohessy-Wiltshire matrices are a system of solutions of the CW differential equations describing a first-order approximation of orbital relative motion, in which the target is in a circular orbit, and the chaser is in an elliptical or circular orbit. Only in this context does a straightforward analytical solution exist. The CW matrices for t = 2 hours = 7,200 seconds and n = 1.2146×10^{-4} rad/s are:

$$[\Phi_{\mathrm{rr}}] = \begin{bmatrix} 4 - 3\cos(\mathrm{nt}) & 0 & 0 \\ 6(\sin(\mathrm{nt}) - (\mathrm{nt})) & 1 & 0 \\ 0 & 0 & \cos(\mathrm{nt}) \end{bmatrix} \tag{30}$$

$$[\Phi_{\mathrm{rr}}] = \begin{bmatrix} 2.0758 & 0 & 0 \\ -0.6436 & 1 & 0 \\ 0 & 0 & 0.6414 \end{bmatrix}$$

$$[\Phi_{rv}] = \begin{bmatrix} \frac{1}{n}\sin(nt) & \frac{2}{n}(1-\cos(nt)) & 0 \\ \frac{2}{n}(\cos(nt)-1) & \frac{1}{n}(4\sin(nt)-3(nt)) & 0 \\ 0 & 0 & \frac{1}{n}\sin(nt) \end{bmatrix} \tag{31}$$

$$[\Phi_{rv}] = \begin{bmatrix} 6.3168\times10^{3} & 5.9051\times10^{3} & 0 \\ -5.9051\times10^{3} & 3.6672\times10^{3} & 0 \\ 0 & 0 & 6.3168\times10^{3} \end{bmatrix}$$

$$[\Phi_{vr}] = \begin{bmatrix} 3n(\sin(nt)) & 0 & 0 \\ 6n(\cos(nt)-1) & 0 & 0 \\ 0 & 0 & -n\sin(nt) \end{bmatrix} \tag{32}$$

$$[\Phi_{vr}] = \begin{bmatrix} 2.7954\times10^{-4} & 0 & 0 \\ -2.6132\times10^{-4} & 0 & 0 \\ 0 & 0 & -9.3182\times10^{-5} \end{bmatrix}$$

$$[\Phi_{vv}] = \begin{bmatrix} \cos(nt) & 2\sin(nt) & 0 \\ -2\sin(nt) & 4\cos(nt)-3 & 0 \\ 0 & 0 & \cos(nt) \end{bmatrix} \tag{33}$$

$$[\Phi_{vv}] = \begin{bmatrix} 0.6414 & 1.5344 & 0 \\ -1.5344 & -0.4344 & 0 \\ 0 & 0 & 0.6414 \end{bmatrix}$$

The velocities at the beginning and end of the rendezvous path, (δv_0^{+}) and (δv_f^{-}), are found with

$$(\delta \mathrm{v}_0^+) = -[\Phi_{rv}(t_f)]^{-1}[\Phi_{rr}(t_f)](\delta \mathrm{r}_0) \tag{34}$$

$$(\delta \mathrm{v}_f^-) = [\Phi_{vr}(t_f)](\delta r_0) + [\Phi_{vv}(t_f)](\delta \mathrm{v}_0^+) \tag{35}$$

The Δv at the beginning of the rendezvous maneuver is found as

$$(\Delta \mathrm{v}_0) = (\delta \mathrm{v}_0^+) - (\delta \mathrm{v}_0^-) \tag{36}$$

$$(\Delta \mathrm{v}_0) = \begin{pmatrix} 3.3977 \times 10^{-11} \\ 5.0259 \times 10^{-11} \\ 2.6380 \times 10^{-5} \end{pmatrix} - \begin{pmatrix} -3.4550 \times 10^{-11} \\ 1.9948 \times 10^{-11} \\ -1.8218 \times 10^{-5} \end{pmatrix}$$

$$(\Delta \mathrm{v}_0) = \begin{pmatrix} -5.7316 \times 10^{-13} \\ 7.0207 \times 10^{-11} \\ 8.1621 \times 10^{-6} \end{pmatrix} \text{ km/s}$$

The Δv at the conclusion of the rendezvous maneuver is

$$(\Delta \mathrm{v}_f) = (\delta \mathrm{v}_f^+) - (\delta \mathrm{v}_f^-) \tag{37}$$

$$(\Delta \mathrm{v}_f) = \begin{pmatrix} 0 \\ 0 \\ 0 \end{pmatrix} - \begin{pmatrix} 3.0040 \times 10^{-11} \\ -9.5860 \times 10^{-12} \\ 4.1130 \times 10^{-5} \end{pmatrix}$$

$$(\Delta \mathrm{v}_f) = \begin{pmatrix} -3.0040 \times 10^{-11} \\ 9.5860 \times 10^{-12} \\ -4.1130 \times 10^{-5} \end{pmatrix} \text{ km/s}$$

The total Δv requirement is

$$\Delta v_{total} = \|\Delta \mathrm{v}_0\| + \|\Delta \mathrm{v}_f\| \tag{38}$$

$$\Delta v_{total} = (8.1621 \times 10^{-6}) + (4.1130 \times 10^{-5}) \text{ km/s}$$

$$\Delta v_{total} = 4.93 \times 10^{-5} \text{ km/s}$$

$$\Delta v_{total} = 0.0493 \text{ m/s}$$

The full range of Δvs for the return leg was simulated in MATLAB with the algorithm described in Equations 16-38 and found to range between 20.26 cm/s at 74,000 km and 4.93 cm/s at 137,000 km. This remains true while both spacecraft share the same argument of periapsis (ω). Constant hover-thrusting will change the ω of the mothership, leading to an exponential increase in Δv for rendezvous maneuvers. This makes it difficult for the daughtercraft to attempt rendezvous when its relative ω to the mothership is large. An implementation of this algorithm in MATLAB is given in Appendix B.

If the daughtercraft are deployed to any Saturn-centric radius different from that of the mothership, there will be an induced secular separation due to Keplerian shear. This would make returning to the mothership difficult for sorties of significant time duration. For this reason, obstacle-avoidance maneuvers should avoid changing the Saturn-centric radius as much as possible (Section 3.4.2).

The low Δv requirement makes it possible for electric propulsion to be considered for the two-impulse rendezvous scenario with nonimpulsive thrusting without needing to use more advanced estimating methods such as the Runge-Kutta approximation. The trade-off between electric and chemical propulsion is detailed in Section 3.4.3.

3.4.2 Obstacle localization and avoidance

From Cassini radio observations of the main rings, the particle diameters range from a few cm to tens of meters, and the mean distance between particles is a few meters. The relative velocity between particles is on the order of a few mm/s, so a spacecraft capable of mm/s Δvs on short notice should be able to avoid them [63].

Successful obstacle avoidance requires the ability to detect the ring particles within 4π steradians and a radius of several meters, implying the use of one field-of-view (FOV) cone on each face of the spacecraft. Existing LIDAR hardware have too large footprints (>1 kg) to fit within all six faces of a 6U CubeSat with all the other systems included [71]. An alternative is to use millimeter-wave radar that can be emitted and tracked with small low-power chips. Millimeter-wave radar cannot sense the shape and structure of target objects, nor detect any that are under a few mm diameter, but it can accurately detect motion even at mm/s velocities [72]. The output from the radar sensors would be autonomously processed into thrust vectors on-board the daughtercraft, eliminating the light-speed delay imposed by the need to coordinate with ground control.

The daughtercraft would not be sent into the parts of the rings that have a high packing density such that transit becomes impossible, such as the B ring core. This scenario may require the use of chip-sized spacecraft, which are outside the scope of this thesis.

3.4.3 Electric and chemical propulsion

The small volume of the daughtercraft precludes more than one propulsion system from being used. The choice of propulsion system depends on not just Δv, but also on the scalability of the overall system to handle both the inclination-change and the obstacle avoidance tasks with the least footprint possible.

Existing chemical thrusters for CubeSats offer quick acceleration at the cost of low specific impulse, which results in propellant tanks that take up a substantial (0.5U to 1U) volume of the spacecraft. They also cannot be scaled down to the mm/s Δv required for obstacle avoidance. Ion and electrospray thrusters exist for CubeSats at power levels of 5.5-15 W [73][74][75], but with footprints that preclude their use as lateral thrusters. The optimal electric propulsion solution for SIREN was found to be the electrospray micro-thruster, which has low enough power and volume requirements for multiple units to be used on each daughtercraft. Its ionic liquid propellant does not require pressurization, and can be fed into the thruster by capillary action. Each thruster has its own propellant tank with a volume of >1 cc each [76].

A single prototype Precision Electrospray Thruster Assembly (PETA) based on the above-mentioned thrusters is capable of providing 100 μN of thrust at 3.2 W, with a specific impulse of at least 1700 seconds [76]. For avoiding ring particles that require Δvs of 1 to 10 mm/s, the burn time would be 100 to 1000 seconds for a 10 kg spacecraft.

For inclination-change maneuvers with higher Δvs, higher thrust levels are recommended to minimize the burn time. Proportionally, 800 μN of thrust would require 25.6 W of power. For the 3.64 cm/s inclination change at 137,000 km, the burn would take 7.58 minutes and 0.0218 grams of propellant. The energy figures for propulsion in Section 5.1 assume 6 hours of thrusting per sortie to cover all maneuvers.

3.4.4 Thermal environment & control

The spacecraft bulk temperature around Saturn is dictated by the local solar flux, absorptivity (α) to emissivity (ϵ) ratio of the surfaces, and heat dissipation inside the spacecraft. The steady state bulk temperature T is best estimated by summing all the heat inputs and outputs at each phase of the orbit, according to Equation 39:

$$\text{Internal heat dissipation} + S\alpha A_x + VF(\epsilon\sigma A_x T_{saturn}^4) + VF(S\alpha A_x)(\text{albedo}) = \sigma\epsilon A_s T^4 \tag{39}$$

where the solar flux S is 14.7 W/m^2, the albedo is 0.342 and Saturn's blackbody temperature, T_{saturn}, is 81 K [77]. A_x is the spacecraft cross-sectional area and A_s is the spacecraft total surface area. VF is the view factor between Saturn and the face of the spacecraft pointing towards it, modeled as a flat plane perpendicular to the Saturn vector in Equation 40 [78]:

$$VF = \left(\frac{r_s}{r}\right)^2 \tag{40}$$

where r_s is the equatorial radius of Saturn (60,268 km), and r is the orbital radius.

The albedo and planetary infrared contributions to the spacecraft heat balance are negligible, regardless of orbital radius. The steady-state bulk temperature is thus dominated by the amount of heat dissipated inside the spacecraft, with a contribution from the Sun exposure/eclipse periods in Saturn orbit. The eclipse period is in turn determined by the beta angle of the spacecraft orbit to the solar vector (Section 3.3.3). In this case, the orbit of the spacecraft is in nearly the same inclination as the ring plane so the beta angle equals the axial tilt of the ring plane to Saturn's orbital plane around the sun, which is 26.7 degrees (0.4665 radians) at its maximum during the solstices, and 0 degrees at minimum during the equinoxes [77].

The above analysis assumes that each spacecraft is completely covered in thermal control coatings, which is unlikely to be the case. The emissivities of the thrusters, antennas, and instrument openings must also be taken in account. The MEMS electrospray thrusters and antennas have a covering of pure silicon or silicon-on-sapphire, which has an emissivity of ~0.5 [79]. The instrument apertures are assumed to be of glass (emissivity = 0.95 [80]).

Modeling the thruster area as 1.2 by 1.2 cm by 56 thrusters (Section 5.4), and the body-mounted antenna area as 2×10 cm^2, the total silicon area is 0.0101 m^2, or 4.6% of the total spacecraft surface area. The instrument apertures were modeled as 6 circles 1 inch (2.54 cm) in diameter, for a surface area of 0.003 m^2 (1.4% of the total surface area). The radiating flux side of Equation 40 was modified to take these in account, with three separate ϵA terms.

$$flux_{radiating} = \sigma(\epsilon_{th}A_{th} + \epsilon_{Si}A_{Si} + \epsilon_{glass}A_{glass})T^4 \tag{41}$$

The greater and more constant the internal heat dissipation, the more the spacecraft must rely on high-emissivity coatings to passively remove excess heat. For low heat dissipation (~5 W), an α/ε ratio of 9.5 with an ε of 0.02 results in a bulk temperature of 295 K (22 C). This relationship was not affected by the orbital radius. For larger antenna and aperture areas, the internal heat dissipation can be increased to compensate, and vice versa.

3.4.5 Power generation & energy storage

Under the assumption that solar power is not used due to low solar flux and difficulty of maneuvering between the ring particles, batteries and/or small radioisotope power sources (RPS) would be used. To minimize mass, the highest specific-energy batteries available will be assumed for this analysis. If each spacecraft is considered expendable, primary Li-$SOCl_2$ batteries would be used, with an energy density of 410 W-hr/kg [81]. If the spacecraft are recoverable, rechargeable Li-Po batteries with an energy density of 172 W-hr/kg would be used [82].

The daughtercraft are estimated to use at least 5-10 W continuously. From Tables 3.2-3.4 in Section 3.5.1, a baseline energy use of 550 W-hr was selected. For Li-$SOCl_2$ batteries, the required mass comes in at 1.34 kg. The equivalent Li-Po battery would mass 3.2 kg. Combined with the mass of all the other subsystems, the Li-Po battery would push the total spacecraft mass over 10 kg unless descoping options to other systems are considered.

Balint et al [83] provides several small thermoelectric RPSs that have been designed for missions with low power demands that cannot benefit from solar power. They range from small RPSs that run on a single Radioisotope Heater Unit (RHU) to larger ones that run on General Purpose Heat Sources (GPHS). The heating is caused by the radioactive decay of Pu-238, and the resulting temperature gradient across the thermocouples is exploited by the Seebeck effect to generate electrical power at low efficiencies. The RHU-based RPSs generate 20-40 mW, not sufficient power to recharge the batteries quickly for the minimum constant power demand during ring operations.

A single GPHS outputs 220 watts (Wt) of heat at end of life (EOL) (Turpin, 2007). Even with high-emissivity coatings, a 6U CubeSat has insufficient surface area to radiate this heat away and keep its bulk temperature within operating ranges of its electronics without adding deployable radiators. However, a whole GPHS uses four PuO_2 pellets. A fractional GPHS at EOL with two pellets would radiate only 110 Wt, of which 101 Wt could be exploited to generate 33 We of electrical power with a Stirling converter at 33% efficiency. This efficiency figure is based on an acceptor temperature of 650 C and a rejector temperature of 120 C, and increases with decreasing rejector temperature [84]. If the cold end could be set to 0 C or below, the overall efficiency of the Stirling engine/alternator would rise high enough to permit power generation of a few tens of watts with only only one PuO_2 pellet, which masses 360 g and radiates 55 Wt at EOL. The combined engine/alternator described in [84] has a specific power of >100 We/kg, enough to generate 30 We with only 300 g. This is unnecessary for most tasks except for sustained thrusting. Any excess power is released as more heat for the thermal control system to reject. The advantages of this power source are obvious since it could eliminate the need for batteries and provide free heating at a lower system mass, but there are still uncertainties due to lack of development and the limited availability of Pu^{238} for use on space missions.

The selection of a plutonium-based power source would require a complete redesign of the thermal control system to dissipate the excess heat, add extra radiation shielding to the electronics, and add at least several million dollars to the mission cost. PuO_2 can be bought from the US Department of Energy at $5840 USD a gram, so a 360-gram pellet would cost $2.1 million USD [85]. Additional costs would come with the extra research and development required to validate a small Stirling radioisotope generator (SRG) within the tight confines of a 6U CubeSat. Given these difficulties and uncertainties, improved battery technology may yield satisfactory results at lower cost and with a shorter development schedule.

3.4.6 Sample return vs. in-situ analysis

Another factor in determining whether the daughtercraft will be recoverable or expendable will be the value of a heavy instrument on the mothership for more extensive sample analysis than the daughtercraft can perform on-site. Using the Sample Analysis at Mars (SAM) instrument suite as an example [86], this suite is much heavier than the daughtercraft can carry without exceeding 10 kg, so basing it on the mothership can help extend the capabilities of the daughtercraft network depending on how much science can be extracted from the ring particles.

The tunable laser spectrometer in the SAM suite would be used to find molecular impurities and isotopes in evolved gases from heating water ice. The SAM suite also uses gas chromatography/mass spectrometry for this purpose.

3.5 Spacecraft

3.5.1 Mothership and daughtercraft overall design

This section is not meant to provide a detailed design of the mothership, but to specify what it needs to do to support the daughtercraft network. The mothership is assumed to be similar to the Saturn Ring Observer design (Nicholson et al, 2010), with the following items:

M1 Gimbaled electric thrusters for hover orbiting and ring traverses
M2 High gain antenna for communications with Earth
M3 Multiple-GPHS RTG for power generation in the hundreds of watts range
M4 LIDAR to determine distance to the ring plane
M5 Wide-angle camera for ring plane imaging
M6 Narrow-angle camera for ring plane imaging

To support the network, several items would be added:

M7 Docking ports or canisterized dispensers for the daughter craft
M8 Low gain, high data rate antennas to support cross-links in the deployed network
M9 Additional flash memory to store the data uploaded from the daughtercraft before transmission to Earth
M10 Magnetic docking ports to recover the daughtercraft. This is done to prevent contamination and damage of the spacecraft surface caused when the daughtercraft fires its thrusters too close to the mothership (optional)
M11 Sample analysis instrument (optional)
M12 Additional propellant tanks for refueling the daughtercraft (optional)

There are several mission requirements that drive the general design of the daughtercraft. At the highest level, the daughtercraft shall have the following abilities to:

D1 survive a cruise of at least seven years (imposed on all subsystems and partially the responsibility of the mothership)
D2 maintain sufficient power for operations away from the mothership
D3 communicate with the mothership at high data rates via low-gain antennas
D4 travel to the intended destination/orbit
D5 achieve precise pointing of its instruments
D6 detect the location of nearby ring particles and avoid them

There are several specific requirements that drive the design of each specialized daughtercraft. The ring particle standoff daughtercraft (SIREN-A) shall have the following abilities to:

A1 take close-up images of the ring particles in the visual spectra, with 10 cm/pixel at 800 meters or better

The ring environment daughtercraft (SIREN-B) shall have the following abilities to:

B1 detect and analyze the composition and distributions of the ions and neutral particles inside the ring plane
B2 detect the magnetic fields and gradients in and out of the ring plane

The ring particle sampling daughtercraft (SIREN-C) shall have the following abilities to:

C1 take high-resolution images of an ice boulder at distances from a few meters to a few millimeters
C2 drill several centimeters into the ice boulder regardless of composition
C3 detect isotopes and impurities on the ice boulder surface
C4 Return an ice core sample to the mothership

Requirement D2 is dependent on the power system, covered in Section 3.5.5. The data rate in requirement D3 is dependent on the size and resolution of the images taken with the cameras on SIREN-A, and -C. The spectrometers would have a much lower data rate, so they do not dominate the communications requirement. The subsystems of each daughtercraft are summarized in Tables 3.2-3.4.

Table 3.2: Mass and power allocations on SIREN-A

Subsystem	*Mass (g)*	*Int. Volume (cm^3)*	*Peak power (W)*	*Energy (W-hr)*
Avionics (2)[1]	1,098	320	10.8	259.2
Science[2]	1000	701.25	20	40
Communications	70	10	3	18 (at 3 W) 1.8 (at 300 mW) 0.6 (at 100 mW) 0.3 (at 50 mW)
Thermal control	11	negligible	N/A	N/A
Power	1,340	670	N/A	N/A
Structure	1,100	N/A	N/A	N/A
Attitude Control[3]	535	506.631	4.25	4.25
Propulsion[4]	665	1,354.752	25.6	153.6
MARGIN (15%)	872.85	534.39495	9.5475	71.2575
TOTAL	6,691.85	4,097.02795	73.1975	546.3075

[1] RAD750 3U [45]
[2] Tables 3.5-3.7
[3] Table 3.8
[4] iEPS thrusters and propellant tanks

Table 3.3: Mass and power allocations on SIREN-B

Subsystem	*Mass (g)*	*Int. Volume (cm³)*	*Peak power (W)*	*Energy (W-hr)*
Avionics (2)	1,098	320	10.8	259.2
Science	760	902.176	2.3	31.2
Extendible/Retractable Boom*	310	500	0.5	1
Communications	70	10	3	18 (at 3 W) 1.8 (at 300 mW) 0.6 (at 100 mW) 0.3 (at 50 mW)
Thermal control	11	negligible	N/A	N/A
Power	1,340	670	N/A	N/A
Structure	1,100	N/A	N/A	N/A
Attitude Control	535	506.631	4.25	4.25
Propulsion	665	1,354.752	25.6	153.6
MARGIN (15%)	883.35	639.53385	6.9675	70.0875
TOTAL	6,772.35	4,903.09285	53.4175	537.3375

*AstroTube [87]

Table 3.4: Mass and power allocations on SIREN-C

Subsystem	*Mass (g)*	*Int. Volume (cm³)*	*Peak power (W)*	*Energy (W-hr)*
Avionics (2)	1,098	320	10.8	259.2
Science	2140	1,230.901	11	127
Communications	70	10	3	18 (at 3 W) 1.8 (at 300 mW) 0.6 (at 100 mW) 0.3 (at 50 mW)
Thermal control	11	negligible	N/A	N/A
Power	1,340	670	N/A	N/A
Structure	1,100	N/A	N/A	N/A
Attitude Control	535	506.631	4.25	4.25
Propulsion	665	1,354.752	25.6	153.6
MARGIN (15%)	1043.85	613.8426	8.1975	84.3075
TOTAL	8,002.85	4,706.1266	62.8475	646.3575

3.5.2 Scientific instruments

Several potential instruments may be considered for placement on each daughtercraft, based on existing and near-term hardware. They are given in Tables 3.5-3.7. All instruments in SIREN-A have a duty cycle of 10% each. They will observe an ice boulder simultaneously during daylight periods.

Table 3.5: SIREN-A Payload Instruments

Payload	*Mass (g)*	*Volume (cm³)*	*Idle/peak power (W)*	*Energy (W-hr)*
Visual camera w/ optics[1]	500	350.625	0/10	40
Second copy for rear-viewing (optional)	500	350.625	0/10	40
TOTAL	1,000	701.25	0/20	80

[1] Mars 2020 EECAM [88]

Each instrument in SIREN-B (Table 6) except for the INMS would have a 100% duty cycle, with the INMS active on command. SIREN-B carries a magnetometer that must be deployed on an extendible/retractable boom up to 3 metres to avoid interference from the daughtercraft electronics. The AstroTube from Oxford Space Systems is one such candidate [87]

Table 3.6: SIREN-B Payload Instruments

Payload	*Mass (g)*	*Volume (cm³)*	*Idle/peak power (W)*	*Energy (W-hr)*
Magnetometer[2]	200	70.176	0/0.7	16.8
Ion & neutral mass spectrometer[3]	560	832	0.6/1.6	14.4
TOTAL	760	902.176	0.6/2.3	31.2

[2] NSS Magnetometer [89]
[3] Compact INMS [90]

Mars Hand Lens Imager (MAHLI) was baselined for SIREN-C to provide high-resolution imaging regardless of distance from the target ice boulder [91]. For surface chemical composition of the ice boulders, an Alpha Particle X-ray spectrometer (APXS) was baselined for

SIREN-C. The APXS used on Rosetta Philae had a mass of 640 grams and an operating power consumption of 1.5 W. It takes a few hours to identify the trace compounds within its target [92].

The thermal drill is based on the Planetary Volatiles Extractor from Honeybee Robotics [36]. In vacuum, water ice undergoes sublimation instead of melting when heated. Assuming an enthalpy of sublimation of 51 kJ/mol [48], it takes 2.83 kJ to sublimate 1 gram of water ice. Losses due to heat conduction in the surrounding ice will increase this figure, but the efficiency of this process can be maximized by using pulses of intense heat to quickly sublimate the ice before the heat is conducted away. The energy to remove 9 grams of ice can be delivered at 7 W-hr for one hour (25.2 kJ), or less at longer drilling times.

Table 3.7: SIREN-C Payload Instruments

Payload	*Mass (g)*	*Volume (cm³)*	*Idle/peak power (W)*	*Energy (W-hr)*
Hand lens[4]	578	790.321	1.75/2.5[7]	42
Thermal drill w/ microspine gripper[5]	500	262.19	0/7	81
APXS[6]	640	178.39	0/1.5	4
TOTAL	1,718	1,230.901	1.75/11	127

[4] MAHLI [91]
[5] Based on Honeybee Robotics Planetary Volatiles Extractor [36]
[6] Klinghofer et al. [92]
[7] MSSS ECAM

The microspine gripper is based on JPL work on cliff robots and asteroid grippers [93]. No mass or energy figures were found for this technology, but a gripper could be designed for a small enough footprint to fit in the spacecraft.

Tunable laser spectrometry (TLS) can be resolution-tuned to specific species in a sample, and offers non-destructive analysis unlike mass spectrometry. It would be primarily used to detect deuterium/hydrogen ratios in water (in the form of HDO/H_2O). Recent advances in TLS suggest a 1-kg device consuming 750 mW of power [52]. If the daughtercraft are recoverable, a heavier version of this instrument can instead be placed on the mothership for the ice core samples SIREN-C brings back.

3.5.3 Common design & structure

The daughtercraft are based on the 6U CubeSat design, with one 1.1-kg aluminum frame in common with each other [94]. These designs were selected chiefly for their ability to be ejected from the dispensers on the mothership, leading to the requirement that most of the surfaces be flush with the interior surfaces of the enclosures. Any protrusions would be kept to a minimum and restricted to the face of the daughtercraft that is exposed to space during storage. The frames also have an internal structure that partition the spacecraft into up to six modules, which is taken in account for the internal volume sums in Tables 3.2-3.4. The outer envelope of each frame is 7705.5 cm^3 (10 by 22.63 by 34.05 cm) and the inner envelope is 4943.5 cm^3 (9.6 by 9.6 by 8.94 cm, multiplied by 6). As shown in Tables 3.2-3.4, the total volume of all subsystems is less than the available internal volume. The volume of the 6U frame is the difference between the outer and inner envelopes, or 2762 cm^3.

The canisterized satellite dispensers detailed in Hevner et al [69] are rectangular-cubic on the inside with rails to guide the payloads during deployment, so the daughtercraft would have similar grooves to minimize vibration inside their dispensers during launch and deep-space maneuvers. The frames are anodized to prevent vacuum welding to the dispenser interior during transit to Saturn.

Figure 3.3: SIREN common bus and payloads

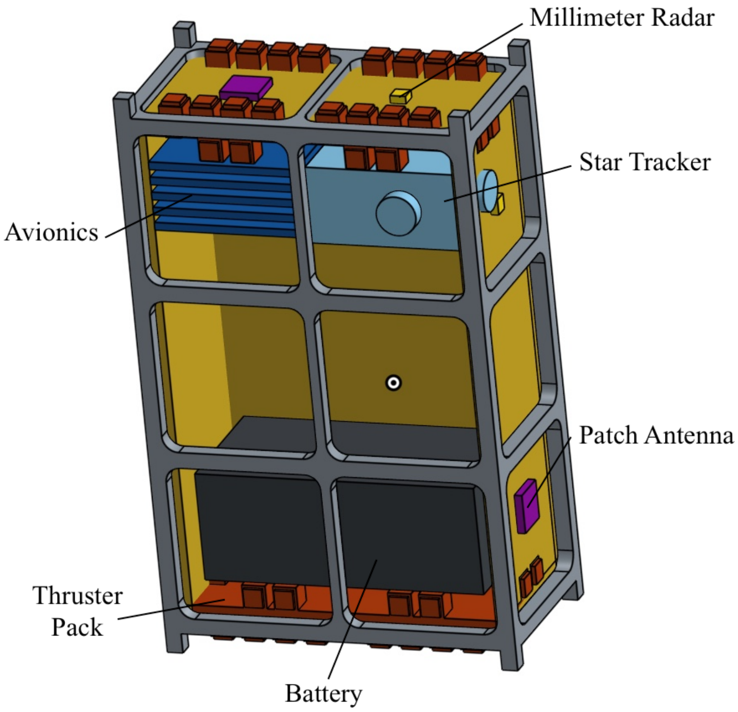

Figure 3.3 shows the common bus of all SIREN variants. Each common bus consists of millimeter-wave radar (Section 3.4.2), two thruster packs (Section 3.5.4), battery (Section 3.5.5), avionics and patch antennas (Section 3.5.7), and a star tracker (Section 3.5.8).

3.5.4 Propulsion

From the trade study done in Section 3.4.3, the electrospray micro-thruster was judged to be the best overall choice for SIREN, with the lowest propellant and volume requirements. Its modular, quasi-cubic form factor allows for easy scalability to fit mission requirements. Clustered thrusters will allow adequate thrust to avoid obstacles and execute inclination changes in a short time frame. For attitude control, the lateral thrusters are located at the edges/vertices of the spacecraft to maximize torque regardless of rotational axis.

For ease of integration, the thrusters are grouped into two thruster boards, one on each end of the spacecraft (Figure 3.4). Each board has integrated circuits and power processing units (PPUs) to support and control the thrusters in any firing configuration. One face has 16 thrusters in four rows, and is used for major orbital maneuvers with Δvs in the range of cm/s to m/s. The opposite face has 12 thrusters facing laterally to handle the obstacle avoidance, pitch, yaw, and roll tasks. Each board thus has 28 thrusters, for a total of 56 thrusters.

Figure 3.4: SIREN Thruster Layout

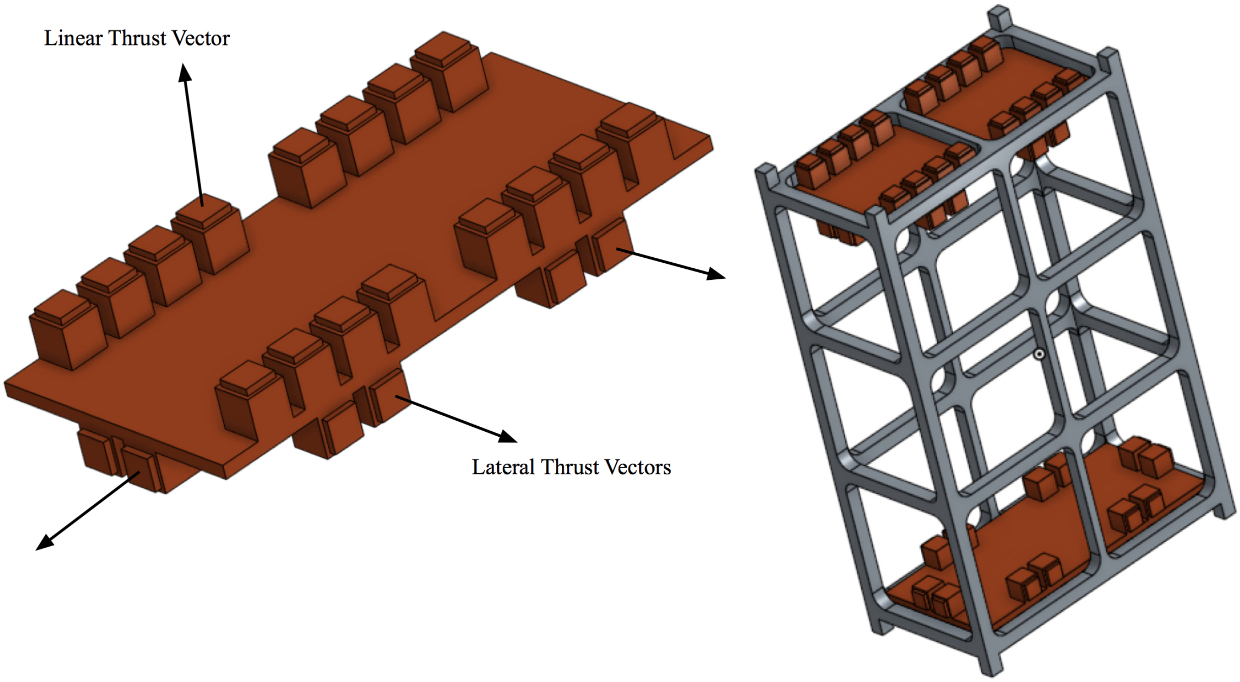

Each thruster can only fire either a positively or negatively-charged stream of ions, and so must be used in charge-opposed pairs to keep the spacecraft neutrally charged. Under the assumption that each PPU supports 8 thrusters, 7 PPUs are sufficient to regulate the propulsion system. Each PPU-thruster module has a dry mass of 95 grams and takes up a volume of 9.6 by 9.6 by 2.1 cm [95]. The entire propulsion system thus masses 665 grams without propellant.

3.5.5 Power subsystem

Due to the uncertainty in Stirling radioisotope generator development (Section 3.4.5), the 1.34-kg $LiSOCl_2$ battery was baselined for SIREN under the assumption that each daughtercraft is expendable. While this battery type has a very high energy density, it has limited power density (<100 W/kg) and suffers a drop in performance at temperatures of -20 degrees Celsius or below [81].

3.5.6 Thermal control subsystem

Due to the limited volume, the entire spacecraft would essentially be designed as a warm-electronics box, with a few cold-tolerant components on the exterior. Table 3.8 shows many of the overlapping temperature ranges of each component. The instruments, thruster assemblies, and batteries are the components most sensitive to cold, so they would receive electrical heating during periods of dark or low use.

Table 3.8: Temperature Ranges of Spacecraft Components (SIREN)

Component	*Allowable flight temperatures (K)*	
	Operational	*Survival*
CPU[1]	258 to 318	243 to 333
Antennas[2]	173 to 373	153 to 393
Batteries[3]	233 to 343	-
Thrusters[4]	263 to 353	233 to 373
Propellant[5]	assumed similar to thrusters	-
Cameras[6]	218 to 323	138 to 343

[1] [58], p.348
[2] [57], p. 428
[3] $LiSOCl_2$ [81]
[4] TILE-1 [96]
[5] Ionic liquid
[6] Mars 2020 EECAM [88]

A few layers of multi-layer insulation (MLI) is sufficient to retard heat loss to space at Saturn (Smith et al, 2016), with the outer layer coated in vapor-deposited gold with an absorptivity/emissivity ratio above 9. At this ratio, the bulk temperature of the spacecraft is 305-308 K when 5 W is internally dissipated, regardless of sunlight. The exoskeletal frame of the spacecraft is anodized aluminum with a high emissivity [97], so it can be used as a heat sink to dampen periods of excessive internal heat dissipation.

This thermal design is a departure from what spacecraft normally use. 10-15 layers of MLI is typical, but there is a small gap between each layer, so the thickness of a typical MLI blanket quickly becomes prohibitive for a CubeSat. In a thermal analysis of the MIST satellite [98], a two-layer model was compared to a ten-layer model in Siemens NX, with an unheated aluminium box inside the MLI shell. In the thermal environment around Ganymede, the two-layer model resulted in a temperature difference of only 0.3 degrees Celsius from the ten-layer model. This temperature difference widened to 1.3 degrees Celsius for the Mercury thermal scenario. The extrapolation from these two scenarios is that a thermal scenario at the Saturnian rings will result in a even narrower temperature difference. Adding more layers of MLI brings diminishing returns on insulation value, caused by heat conduction between the layers through their spacers.

Another way to reduce MLI mass and volume is to incorporate it into the structure. This is done with structural MLI (S-MLI), which has been tested and validated at Tethers Unlimited [99]. Instead of fragile thin films, each layer is constructed with 3D-printing techniques and there is a rigid outer layer strong enough to support antennas and other surface-mounted components.

3.5.7 Communications and data handling

For a CubeSat mission, the mass and data rates of the communications hardware are severely restricted. A mitigating factor is that the daughtercraft are assumed to be within line-of-sight with the mothership at all times with a separation of no more than two kilometers, so free space losses in the crosslinks are expected to be tolerable with low-gain ultra-high frequency (UHF) antennas.

UHF micro-transceivers have been introduced that mass less than 50 g, measure 10 cm^3, and consume less than 1 W of power [59]. They are cold- and radiation-tolerant, allowing them to be placed outside warm-electronics boxes and shielding. For these particular micro-transceivers, commands can be received at 2 or 8 kbps and science data transmitted at 100 kbps at 1 W, provided there is a clear line of sight between the daughtercraft and the mothership. At this rate, a 20-Mb photograph from one of the visual cameras can be transmitted in 3.3 minutes assuming a typical compression of 4 bits per pixel (subframing each photograph down to 1024 by 1024 pixels would reduce the file size to 4 Mb).

Nicholson et al [67] specified a rate of 1 image per minute for the Saturn Ring Observer concept study, to best capture the motion and rotation of the ring particles. Crosslinking this image rate from the daughtercraft to the mothership would require 333.33 kbps, achievable with 4 100-kbps antennas or by increasing the power to each antenna.

2 Gb of flash memory is sufficient to hold 100 20-Mb images with no power consumption. The MSL RAD750-3U board with the above modification is baselined for the avionics suite, with two units for redundancy. Due to the short crosslink distance, data could be uploaded to the mothership almost as quickly as it is generated, reducing the need to store science data on the daughtercraft for long periods of time.

3.5.8 Attitude control

Owing to the lack of need for Earth-pointing and proximity to the Saturnian magnetic field, the SIREN attitude control system design would be greatly simplified compared to that for Cassini. The electrospray thrusters meant for obstacle avoidance (Section 3.5.4) have a low enough thrust to be used for precision attitude control, eliminating the need for gyros and reaction wheels that would otherwise take up volume within each daughtercraft and simplifying the overall spacecraft design.

The region of the Saturnian magnetosphere that is co-located within the rings is strongly dipolar with a field strength of 21 μT, comparable to the geomagnetic field strength in LEO [100]. This makes a small magnetorquer particularly attractive for orienting the spacecraft parallel to the magnetic field lines and perpendicular to the ring plane before the inclination-change burn. A star tracker and sun sensor are included in the attitude control suite in each daughtercraft, which is given in Table 3.9.

Table 3.9: SIREN Attitude Control System Components

Component	*Mass (g)*	*Volume (cm³)*	*Idle/peak power (W)*	*Energy (W-hr)*
Magnetorquer[1]	30	4.453	0.2	0.2
Star tracker[2]	500	500	4	4
Sun sensor[3]	5	2.178	0.05	0.05
TOTAL	535	506.631	4.25	4.25

[1] CubeSat Magnetorquer Rod [101]
[2] MIST [102]
[3] CubeSat Sun Sensor [103]

3.6 Discussion

As discussed in the previous sections, a 6U CubeSat network supported by a mothership has the potential to efficiently explore the structures and particles along the radial direction of the Saturnian rings. There are several trades that are yet to be resolved, pending certain technological advances in computing and power conversion.

The decision to make the daughtercraft expendable or recoverable depends on the scope of the mission, propulsion capability, depth of science to be returned, and the availability of technologies that enable spacecraft recovery. If SIREN is meant to explore only a thin sliver of the rings at a given orbital radius, expendable daughtercraft may be acceptable. On the other hand, there will be pressure to make the daughtercraft recoverable if the mothership is capable of traversing a wide range of orbital radii. If they are still expendable in this case, the combined mass of duplicate daughtercraft will quickly become prohibitive.

The improvement of small high-efficiency radioisotope generators running on the Stirling cycle will make it easier for mission designers to select recoverability as a design driver for the daughtercraft. As of 2003, small Stirling generators have continuously operated for at least 60,000 hours without maintenance (Wood & Lane, 2003) so moving-part failure is a minor concern. The known footprints of existing hardware seems to suggest a lower system mass than a primary battery, but the mass of shielding, shunt heaters, and other hardware associated with a small SRG is unknown. Further development of small SRGs is desirable for this mission because it offers higher power levels without the need to store energy, leading to a higher operational tempo without the need for power management. This is crucial for the computer processing tasks SIREN must carry out for obstacle avoidance. Additionally, the continuous heat from the radioisotope source would give the spacecraft the ability to prevent small ice particles from clumping onto its outer surfaces.

The changing of the mothership ω during hover-thrusting will drive up the Δv needed for rendezvous, unless the daughtercraft can linger in the rings until their ω lines up with that of the mothership, implying that they stay in the rings for much longer than their batteries would allow.

The presence of multiple ice particles at sizes ranging from <1 cm to >1 m demands the development of spacecraft avionics that can handle machine vision and autonomous tasks with only high-level commands from the controllers. This implies processing speeds more in line with advanced commercial hardware instead of radiation-hardened avionics (Ginosar, 2012). Observations from Cassini have shown that the rings absorb much of the local radiation (Gombosi et al, 2009), removing the need for additional radiation hardening.

4 Conclusions

A mission design was presented that would allow the long-range mobility of a scientific payload on Mars in the 2021 timeframe. Such a probe would advance our understanding of the climate history of the Martian atmosphere as recorded in the polar ice layers, and represents a specialised niche in which balloons are the ideal choice for achieving a planetary exploration objective. The proposed design masses less than 20 kg, making it relatively easy to float in the Martian atmosphere, and to decelerate in the upper atmosphere prior to deploying the balloon.

The current state of the art of tunable laser spectroscopy can be integrated into the presented design, with some miniaturisation. All other instruments and avionics are available to be flown on this mission in their present SOA. The 2021 timeframe presents some challenge, but this proposal does not demand radical technological advancements to become a reality.

Another mission design was presented that would allow in-situ sampling of the Saturn rings within the next few decades. Such a probe would advance our understanding of the history of the rings as recorded in the composition of its particles, and represents a specialized niche in which CubeSats are the ideal choice for achieving a planetary exploration objective. The proposed design masses less than 10 kg per daughtercraft, making it relatively easy to maneuver between the ring particles without a severe expenditure in propellant.

The current state of the art of scientific instruments can be integrated into the presented design. Spacecraft avionics capable of machine-vision and autonomous operations will have to be tested and qualified, but this is not a radical demand for the 2030-2040 timeline.

This thesis contributes to the growing body of planetary mission designs that has been submitted by various researchers from several NASA centers, other governmental space agencies, and private organizations such as the Planetary Society. On the scientific side, it was meant to address gaps in future studies of the Martian north polar cap and the Saturnian rings, which are regions of high science potential. On the technical side, it explored how a small spacecraft architecture can fit within given power and thermal limits in both the inner and outer solar system.

5 Future Work

For HYPATIA to successfully pass the NASA Discovery selection in the coming years, a thorough testing regime will be needed to validate katabatic-wind propulsion at an Earthly location such as Antarctica.

In the case that balloon propulsion by katabatic wind is found infeasible, there are several alternatives worth exploring. Previous work has been done on wind-driven tumbleweed rovers and land-sailing rovers for use on Mars. A balloon-rover hybrid with the balloon towing a two-wheeled chariot payload has been tested by Pioneer Astronautics [104]. An future iteration of HYPATIA might use the latter method of locomotion to travel across the NPLD nearly as quickly as a pure balloon and brake much more easily, without the need to procure lifting gas from the ice. Since the requirement to float would be eliminated, the landed mass could be heavier and support a larger science and communications payload. Should this method be chosen, the increased mass has the potential to change the preferred method of balloon deployment, from aerial deployment to a more complex deployment on the surface. Alternatively, the aerial deployment option could be preserved by having the balloon soft-land the rover on the surface.

A major hurdle towards realization of either mission is the automated navigation software that would convert readings from mm-wave radar sensors into thrust vectors (SIREN) or balloon vent commands (HYPATIA). This was considered out of the scope of this thesis, but this is a good starting point for computer science researchers.

For both missions, a thorough thermal model is needed to advance the design beyond the bulk temperature estimates. This model would take in account the heat dissipation of all power-drawing components, structural MLI layers, absorptivity and emissivity, and additional aerogel insulation in order to identify areas where the temperature is higher or lower than the bulk temperature and how it affects component performance.

References

[1] NASA Small Spacecraft Technology State of the Art [online] https://www.nasa.gov/sites/default/files/atoms/files/small_spacecraft_technology_state_of_the_art_2015_tagged.pdf (accessed 2 January 2017)

[2] CubeSat Design Specification [online] https://static1.squarespace.com/static/5418c831e4b0fa4ecac1bacd/t/56e9b62337013b6c063a655a/1458157095454/cds_rev13_final2.pdf (accessed 8 December 2017)

[3] Keck Institute of Space Studies, 'Small satellites: A revolution in space science', California Institute of Technology, Pasadena, CA, July 2014

[4] NRC/Space Studies Board, 'Briefing to Committee on Achieving Science Goals with CubeSats', 22 June 2015 [online] http://sites.nationalacademies.org/cs/groups/ssbsite/documents/webpage/ssb_166651.pdf (accessed 2 January 2017)

[5] Frazier, W., Rohrschneider, R. and Verzuh, M. (2013) 'Cubesat strategies for long-life missions', *Low Cost Planetary Mission Conference*, 18–20 June, Pasadena, CA.

[6] Klesh, A., Baker, J., Castillo-Rogez, J., Halatek, L., Murphy, N., Raymond, C., Bellardo, J., Cutler, J., Lightsey, G., 'INSPIRE: Interplanetary nano spacecraft pathfinder in relevant environment', AIAA 2013-5323

[7] Asmar, S., Matousek, S., 'Mars Cube One (MarCO): Shifting the paradigm in relay deep space operations', AIAA 2016-2483

[8] McNutt, L., Johnson, L., Clardy, D., Castillo-Rogez, J., Frick, A., Jones, L., (2014) ’Near-Earth Asteroid Scout’, [online] https://ntrs.nasa.gov/archive/nasa/casi.ntrs.nasa.gov/20140012882.pdf (retrieved 12 December 2017)

[9] Cohen, B., ‘Lunar Flashlight: Mapping Lunar Surface Volatiles Using a CubeSat’, FISO Telecon, 22 April 2015 [online] http://images.spaceref.com/fiso/2015/042215_barbara_cohen_nasa_msfc/Cohen_4-22-15.pdf (accessed 2 January 2017)

[10] Clark. P.E., Malphrus, B., Reuter, D., Hurford, T., MacDowall, R., Petro, N., Farrell, W., Brambora, C., Patel, D., Banks, S., Coulter, P., ‘Broadband InfraRed Compact High-resolution Exploration Spectrometer: Lunar Volatile Dynamics for the Lunar Ice Cube Mission’, August 2016 [online] http://digitalcommons.usu.edu/cgi/viewcontent.cgi?article=3474&context=smallsat (accessed 2 January 2017)

[11] Swartwout, M., ‘Twenty (plus) years of University-class Spacecraft: A Review of what was, an Understanding of what is, and a look at what should be next’, 20th Annual AIAA/USU Conference on Small Satellites [online] https://digitalcommons.usu.edu/cgi/viewcontent.cgi?referer=https://www.google.ca/&httpsredir=1&article=1532&context=smallsat (retrieved 13 December 2017)

[12] Weiss, J., Smythe, W., Lu, W., ‘Science Traceability’, IEEE Aerospace Conference 2005, doi:10.1109/aero.2005.1559323

[13] Rainey, L., ‘Space Modeling and Simulation’ (2004). Retrieved from https://arc.aiaa.org/doi/book/10.2514/4.989155

[14] TRL Definitions, [online] https://www.nasa.gov/pdf/458490main_TRL_Definitions.pdf (retrieved 13 December 2017)

[15] McEwen, A. et al. (2007) ‘Mars reconnaissance orbiter’s high resolution imaging science experiment (HiRISE)’, *J. Geophys. Res.*, Vol. 112, No. E5, E05S02, doi: 10.1029/2005JE002605.

[16] Wolf, A., Beegle, L., Raymond, C., Plaut, J., Pollard, B., Gim, Y., Wu, X. and Hall, J. (2012) ‘Mars balloon science’, *Concepts and Approaches for Mars Exploration*, Abstract #4294, Lunar and Planetary Institute, Houston, TX.

[17] Hall, J., Pauken, M., Kerzhanovich, V., Walsh, G., Fairbrother, D., Shreves, C. and Lachenmeier, T. (2007) ‘Flight test results for aerially deployed Mars balloons’, *AIAA Balloon Systems Conference*, 21–24 May 2007.

[18] Aharonson, O., Zuber, M., Smith, D., Neumann, G., Feldman, W., Prettyman, T. (2004) ‘Depth, distribution, and density of CO_2 deposition on Mars’, *Journal of Geophysical Research*, Vol. 109, No. E5, doi:10.1029/2003JE002223.

[19] Hansen, C.J., Byrne, S., Portyankina, G., Bourke, M., Dundas, C., McEwan, A., Mellon, M., Pommerol, A. and Thomas, N. (2013) ‘Observations of the northern seasonal polar cap on Mars: I. Spring sublimation activity and processes’, *Icarus*, Vol. 225, No. 2, pp.881–897, doi:10.1016/j.icarus.2012.09.024.

[20] Levrard, B., Forget, F., Montmessin, F. and Laskar, J. (2004) ‘Recent ice-rich deposits formed at high latitudes on Mars by sublimation of unstable equatorial ice during low obliquity’, *Nature*, Vol. 431, No. 7012, pp.1072–1075.

[21] Smith, I., Holt, J., Spiga, A., Howard, A. and Parker, G. (2013) ‘The northern spiral troughs of Mars as cyclic steps’, *Journal of Geophysical Research: Planets*, Vol. 118, No. 9, pp.1–23, doi:10.1002/jgre.20142.

[22] Fishbaugh, K. and Head, J. (2001) ‘Comparison of the north and south polar caps on Mars: new observations from MOLA data and discussion of some outstanding questions’, *Icarus*, Vol. 154, No. 1, pp.145–161, doi:10.1006/icar.2001.6666.

[23] Mousis, O. et al. (2012) ‘Volatile trapping in Martian clathrates’, *Springer Space Science Review*, Vol. 174, Nos. 1–4, pp.213–250, doi:10.1007/s11214-012-9942-9.

[24] Moores, J.E., Brown, R.H., Lauretta, D.S. and Smith, P.H. (2012) ‘Experimental and theoretical simulation of sublimating dusty water ice with implications for D/H ratios of water ice on comets and Mars’, *Planetary Science*, doi:10.1186/2191-2521-1-2.

[25] Holt, J.W., Fishbaugh, K.E., Byrne, S., Christian, S., Tanaka, K., Russell, P.S., Herkenhoff, K.E., Safaeinili, A., Putzig, N.E. and Phillips, R.J. (2010) ‘The construction of Chasma Boreale on Mars’, *Nature*, Vol. 465, No. 7297, pp.446–449, doi:10.1038/nature09050.

[26] Clancey, W.J. (2012) *Working on Mars: Voyages of Scientific Discovery with the Mars Exploration Rovers*, MIT Press, Cambridge, MA.

[27] Becerra, P., Byrne, S., Sori, M., Sutton, S., Herkenhoff, K., ‘Stratigraphy of the north polar layered deposits of Mars from high resolution topography’, Journal of Geophysical Research: Planets, Vol. 121, No. 8, pp. 1445-1471

[28] Manning, R. and Adler, M. (2005) ‘Landing on Mars’, *AIAA Space 2005 Conference*, September, AIAA-2005-6742, Long Beach, California.

[29] Klell, M. (2015) *Storage of Hydrogen in the Pure Form* [online] http://www.wiley-vch.de/books/ sample/3527322736_c01.pdf (accessed 12 November 2015)

[30] Cantor, B., James, P. and Calvin, W. (2010) 'MARCI and MOC observations of the atmosphere and surface cap in the north polar region of Mars', *Icarus*, Vol. 208, No. 1, pp.61–81. Centro de Astrobiologia (2015) *MSL Rover Environmental Monitoring Station* [online] https://cab.inta-csic.es/rems/intrument-description/ (accessed 9 November 2015).

[31] Mars24 Algorithm and Worked Examples (2014) NASA Goddard Institute for Space Studies [online] http://www.giss.nasa.gov/tools/mars24/help/algorithm.html (accessed 10 June 2014).

[32] Howard, A. (2000) 'The role of eolian processes in forming surface features of the Martian polar layered deposits', *Icarus*, Vol. 144, No. 2, pp.267–288, doi:10.1006/icar.1999.6305.

[33] NSSDC (2015) *NSSDC Mars Fact Sheet* [online] http://nssdc.gsfc.nasa.gov/planetary/factsheet/ marsfact.html (accessed 15 September 2015).

[34] Mischna, M. and Richardson, M. (2005) 'A reanalysis of water abundance in the Martian atmosphere at high obliquity', *Geophysical Research Letters*, Vol. 32, No. 3.

[35] Lahayne, O., Pichler, B., Reihsner, R., Eberhardsteiner, J., Sus, J., Kim, D., Nam, S., Paek, H., Lorenz, B., Persson, B., (2016) 'Rubber Friction on Ice: Experiments and Modeling', [online] https://link.springer.com/content/pdf/10.1007%2Fs11249-016-0665-z.pdf (retrieved 13 December 2017)

[36] Zacny, K., Luczek, K., Paz, A., Hedlund, M., 'Planetary Volatiles Extractor (PVEx) for In Situ Resource Utilization (ISRU)', 15th Biennial ASCE Conference, Earth and Space 2016, DOI: 10.1061/9780784479971.037

[37] Long, S.M., You, T., Halsell, C.A., Bhat, R.S., Demcak, S.W., Graat, E.J., Higa, E.S., Highsmith, D.E., Mottinger, N.A. and Jah, M.K. (2007) *Mars Reconnaissance Orbiter*

Aerobraking Daily Operations and Collision Avoidance, Jet Propulsion Laboratory [online] http://issfd.org/ISSFD_2007/3-3.pdf (accessed 16 November 2015).

[38] Review of the MEPAG Report on Mars Special Regions [online] https://www.nap.edu/catalog/21816/review-of-the-mepag-report-on-mars-special-regions (retrieved 11 December 2017)

[39] Categories of Planetary Protection, [online] https://planetaryprotection.nasa.gov/about-categories/ (retrieved 11 December 2017)

[40] Herny, C., Masse, M., Bourgeois, O., Carpy, S., Le Mouelic, S., Appere, T., Smith, I., Spiga, A. and Rodriguez, S. (2014) 'Sedimentation waves on the Martian north polar cap: analogy with megadunes in Antarctica', *Earth and Planetary Science Letters*, Vol. 403, pp.56–66.

[41] Smith, I., Holt, J., (2010) 'Onset and migration of spiral troughs on Mars revealed by orbital radar', *Nature*, Vol. 465, pp. 450-453, doi:10.1038/nature09049

[42] Banks, M., Byrne, S., Galla, Kapil, McEwen, A., Bray, V., Dundas, C., Fishbaugh, K., Herkenhoff, K., Murray, B., 'Crater population and resurfacing of the Martian north polar layered deposits', *Journal of Geophysical Research: Planets*, Vol. 115, No. E8, August 2010, doi: 10.1029/2009JE003523

[43] Limaye, A., Aharonson, O., Taylor-Perron, J., (2012) 'Detailed stratigraphy and bed thickness of the Mars north and south polar layered deposits', *Journal of Geophysical Research*, Vol. 117, No. E6, doi:10.1029/2011je003961

[44] Plaut, J., (2011) 'Stratigraphy of the Upper Martian Northern Polar Layered Deposits from Radar, Visible, and Topographic Data', 42nd Lunar and Planetary Science Conference, #2653

[45] RAD750 3U (2015) *BAE Systems* [online] http://www.baesystems.com/download/ BAES_052279/ Space-Products--RAD750-3U-cPCI (accessed 19 August 2015).

[46] R. Hoyt, personal communication, October 4, 2015

[47] Mylar (2015) *Mylar Polyster Film Physical and Thermal Properties* [online] http:// usa.dupontteijinfilms.com/informationcenter/downloads/Physical_And_Thermal_Proper ties.pdf (accessed 3 November 2015).

[48] Jones, J., Saunders, S., Blamont, J. and Yavrouian, A. (1998) 'Balloons for controlled roving/landing on Mars', *IAA Third International Conference on Low-Cost Planetary Missions*, California Institute of Technology, 27 April to 1 May 1998.

[48] Chevrier, V.F. and Rivera-Valentin, E.G. (2014) 'Regolith-atmosphere water vapor transfer on Mars: comparison between Phoenix TECP and MSL REMS data', *Eighth International Conference on Mars*.

[49] Marissen, R. (2011) 'Design with ultra-strong polyethylene fibers', *Materials Sciences and Applications*, Vol. 2, No. 5, pp.319–330, doi:10.4236/msa.2011.25042.

[50] Crisp, D., Kaiser, W., Van Zandt, T., Hoenk, M. and Tillman, J. (1995) 'Micro weather stations for Mars', *Acta Astronautica*, Vol. 35, Supplement 1, pp.407–415.

[51] Gomez-Elvira, J., Armiens, C., Castaner, L., Dominguez, M., Genzer, M., Gomez, F., Haberle, R., Harri, A., Jimenez, V., Kahanpaa, H., Kowalski, L., Lepinette, A., Martin, J., Martinez-Frias, J., McEwan, I., Mora, L., Moreno, J., Navarro, S., de Pablo, M.A., Peinado, V., Pena, A., Polkko, J., Ramos, M., Renno, N.O., Ricart, J., Richardson, M., Rodrieguez-Manfredi, J., Romeral, J., Sebastian, E., Serrano, J., de la Torre Juarez, M., Torres, J., Torrero, F., Urqui, R., Vazquez, L., Velasco, T., Verdasca, J., Zorzano, M. and Martin-Torres, J. (2012) 'REMS: the

environmental sensor suite for the Mars science laboratory rover', *Space Science Review*, Vol. 170, Nos. 1–4, pp.583–640, doi:10.1007/s11214-012-9921-1.

[52] Rafkin, S.C., Nowicki, K., Silver, J. and Stanton, A. (2015) 'A multi-channel tunable laser spectrometer for in-situ measurement of planetary atmospheres', Abstract for *11th Low Cost Planetary Missions Conference*, 9–11 June 2015, Berlin, Germany.

[53] Malin Space Science Systems (2010a) *ECAM – C50* [online] http://www.msss.com/ brochures/ ecam-c50.pdf (accessed 7 August 2015).

[54] Malin Space Science Systems (2010b) *ECAM Optics* [online] http://www.msss.com/ brochures/ xfov.pdf (accessed 7 August 2015).

[55] Spectrolab (2014) *Spectrolab Photovoltaic Products, 28.3% UTJ Solar Cells* [online] http:// www.spectrolab.com/DataSheets/TNJCell/utj3.pdf (accessed 15 September 2015).

[56] Clyde (2015) *Clyde Space Spacecraft Batteries* [online] http://www.clyde-space.com/ products/ spacecraft_batteries (accessed 12 November 2015).

[57] Larson, W. and Wertz, J. (1999) *Space Mission Analysis and Design*, 3rd ed., Microcosm Press, El Segundo, CA, USA.

[58] Pisacane, V. (2008), 'The Space Environment and its Effects on Space Systems', Reston, VA, AIAA

[59] Kuhn, W., Lay, N., Grigorian, E., Nobbe, D., Kuperman, I., Jeon, J., Wong, K., Tugnawat, Y. and He, X. (2007) 'A microtransceiver for UHF proximity links including Mars surface-to-orbit applications', *Proceedings of the IEEE*, Vol. 95, No. 10, October, doi:10.1109/jproc.2007. 905092.

[60] Vision and Voyages for Planetary Science in the Decade 2013-2022 [online] https://solarsystem.nasa.gov/docs/131171.pdf (retrieved 7 June 2017)

[61] Esposito, L., (2010) 'Composition, structure, dynamics, and evolution of Saturn's rings', *Annual Review of Earth and Planetary Science*, Vol. 38, pp. 383-410, doi:10.1146/annurev-earth-040809-152339

[62] Dougherty, M., Esposito, L., Krimigis, T., 'Saturn from Cassini-Huygens', Heidelberg: Springer, eds. 2009, pp. 459-509

[63] Charnoz, S., Dones, L., Esposito, L., Estrada, P., Hedman, M., 'Saturn after Cassini-Huygens', Chapter 17, 2009

[64] Cuzzi, J.N., Estrada, P.R., 'Compositional evolution of Saturn's rings due to meteoroid bombardment'. *Icarus* 132, 1-35 (1998), doi: 10.1006/icar.1997.5863

[65] Canup, R., 'Origin of Saturn's rings and inner moons by mass removal from a lost Titan-sized satellite', *Nature*, Vol. 468, 16 December 2010, doi:10.1038/nature09661

[66] Luhmann, J., Johnson, R., Tokar, R., Ledvina, S., Cravens, T., 'A model of the ionosphere of Saturn's rings and its implications', *Icarus 181 (2006) 465-474* doi:10.1016/j.icarus.2005.11.022

[67] Nicholson, P., Tiscareno, M., Spilker, L., 'Mission concept study: Saturn ring observer study report', Jet Propulsion Laboratory, June 2010

[68] Canup, R.M., Esposito, L.W.: Accretion in the Roche zone—coexistence of rings and ringmoons. Icarus 113, 331–352 (1995)

[69] Hevner, R., Holemans, W., Puig-Suari, J., Twiggs, R., ‘An Advanced Standard for CubeSats’, 25th Annual AIAA/USU Conference on Small Satellites, 13 June 2011

[70] Curtis, H., ‘Orbital Mechanics for Engineering Students, 3rd Edition’, *Elsevier*, 2014

[71] ASC GoldenEye Space LIDAR [online] http://www.advancedscientificconcepts.com/products/portable.html (accessed 31 January 2017)

[72] Wang, S., Song, J., Lien, J., Poupyrev, I., Hilliness, O., ‘Interacting with Soli: Exploring Fine-Grained Dynamic Gesture Recognition in the Radio Frequency Spectrum’, *UIST*, October 16-19, 2016, doi:10.1145/2984511.2984565

[73] Busek BET-100 Electrospray Thruster [online] http://www.busek.com/index_htm_files/70008516F.PDF (retrieved May 30, 2017)

[74] Busek BET-1mN Electrospray Thruster [online] http://www.busek.com/index_htm_files/70008500%20BET-1mN%20Data%20Sheet%20RevH.pdf (retrieved May 30, 2017)

[75] Busek BIT-1 Ion Thruster [online] http://www.busek.com/index_htm_files/70011950%20RevA%20Data%20Sheet%20for%20BIT-1%20Ion%20Thruster.pdf (retrieved May 30, 2017)

[76] Martel, F., Perna, L., Lozano, P., ‘Miniature ion electrospray thrusters and performance tests on CubeSats’, *26th Annual AIAA/USU Conference on Small Satellites*, SSC12-VI-5 (2012)

[77] NSSDC (2017) *NSSDC Saturn Fact Sheet* [online] http://nssdc.gsfc.nasa.gov/planetary/factsheet/saturnfact.html (accessed 11 January 2017)

[78] Radiation Heat Transfer Configuration Factors [online] http://www.thermalradiation.net/indexCat.html (accessed May 30, 2017)

[79] Ravindra, N.M., Pierce, D., Guazzoni, G., Babladi, M., Gokce, O., ’Radiative Properties of Materials of Interest to Thermophotovoltaics’ [online] https://www.researchgate.net/profile/Nuggehalli_Ravindra/publication/281493708_Radiative_Properties_of_Materials_of_Interest_to_Thermophotovoltaics/links/55eb32ff08ae65b6389de995/Radiative-Properties-of-Materials-of-Interest-to-Thermophotovoltaics.pdf (retrieved 14 December 2017)

[80] Mikron, Table of Emissivity of Various Surfaces [online] http://www-eng.lbl.gov/~dw/projects/DW4229_LHC_detector_analysis/calculations/emissivity2.pdf (retrieved September 11, 2017)

[81] JPL D-30268, ‘Energy Storage Technology for Future Space Science Missions’, November 2004 [online] https://solarsystem.nasa.gov/docs/D-30268_A._-_Energy_Storage_Technologies_2004%5B1%5D-%20cleared%20version.pdf (accessed 28 January 2017)

[82] Clark, C., Simon, E., ‘Evaluation of Lithium Polymer Technology for Small Satellite Applications’, [online] https://digitalcommons.usu.edu/cgi/viewcontent.cgi?referer=https://www.google.ca/&httpsredir=1&article=1499&context=smallsat (retrieved 28 January 2017)

[83] Balint, T., Marshall, K., Noravian, H., Randolph, J., Satter, C., Schmidt, G., Shirley, J., ‘Enabling Exploration with Small Radioisotope Power Systems’, *JPL Pub. 04-10*, September 2004

[84] Wood, J., Lane, N., ‘Advanced 35 W Free-Piston Stirling Engine for Space Power Applications’, American Institute of Physics Conference Proceedings, 2003

[85] DOE, Plutonium Certified Reference Materials Price List, [online] https://science.energy.gov/nbl/certified-reference-materials/prices-and-certificates/plutonium-certified-reference-materials-price-list/ (retrieved December 10, 2017)

[86] Mahaffy, P.R., Webster, C.R., Cabane, M. et al. *Space Science Review* (2012) 170:401. doi: 10.1007/s11214-012-9879-z

[87] Dove-Jay, A., 'The Development of a Low Mass Extendible Composite Boom for Small Satellite Applications', [online] https://icubesat.files.wordpress.com/2015/05/icubesat-2015_org_b-3-6_boom_lawton.pdf (retrieved 24 September, 2017)

[88] Staehle, R., Basset, C., McKinney, C., Schwochert, M., Boland, J., 'Flexible camera architecture for generic space imaging applications', [online] http://www.lcpm12.org/wp-content/uploads/2017/08/1110-1130-Staehle.pdf (retrieved 24 September 2017)

[89] CubeSatShop NSS Magnetometer [online] https://www.cubesatshop.com/wp-content/uploads/2016/06/NSS-Magnetometer-1.pdf (accessed 12 December 2016)

[90] Rodriguez, M., Paschalidis, N., Jones, S., Sittler, E., Chornay, D., Uribe, P., Cameron, T., Nanan, B., 'A compact ion and neutral mass spectrometer for cubesat/smallsat platforms', [online] http://digitalcommons.usu.edu/cgi/viewcontent.cgi?article=3268&context=smallsat (accessed 12 December 2016)

[91] Edgett, K., Yingst, R., Ravine, M., Caplinger, M., Maki, J., Ghaemi, F., Schaffner, J., Bell, J., Edwards, L., Herkenhoff, K., Heydari, E., Kah, L., Lemmon, M., Minitti, M., Olson, T., Parker, T., Rowland, S., Schieber, J., Sullivan, R., Sumner, D., Thomas, P., Jensen, E., Simmonds, J., Sengstacken, A., Willson, R., Goetz, W., 'Curiosity's Mars Hand Lens Imager (MAHLI Investigation', Space Science Reviews, June 2012. DOI: 10.1007/s11214-012-9910-4

[92] Klingelhofer, G., Bruckner, J., Duston, C., Gellert, R., Rieder, R., (2007) ’The Rosetta Alpha Particle X-Ray Spectrometer (APXS)’, Space Science Reviews, Vol. 128, Issue 1-4, pp. 383-396, doi:10.1007/s11214-006-9137-3

[93] Parness, A., ‘Anchoring Foot Mechanisms for Sampling and Mobility in Microgravity’, *IEEE, International Conference on Robotics and Automation*, May 9-13, 2011

[94] ISIS 6-Unit CubeSat Structure [online] https://www.isispace.nl/product/6-unit-cubesat-structure/ (accessed 22 January 2017)

[95] Krejci, D., Mier-Hicks, F., Fucetola, C., Lozano, P., Schouten, A., Martel, F., ‘Design and Characterization of a Scalable ion Electrospray Propulsion System’, *Joint Conference of 30th ISTS, 34th IEPC and 6th NSAT*, July 4-10, 2015

[96] Accion Systems TILE-1 [online] https://static1.squarespace.com/static/5446faa2e4b025843cfc 6731/t/56b89b839f72662e5f8f460d/1454939011707/TILE_FlySheet_v2.pdf (accessed 28 January 2017)

[97] Henninger, J., ‘Solar Absorptance and Thermal Emittance of Some Common Spacecraft Thermal Control Coatings’, NASA Reference Publication 1121, April 1984

[98] Berggren, A., (2015) ‘Design of Thermal Control System for the Spacecraft MIST’ (Master’s thesis) [online] https://www.diva-portal.org/smash/get/diva2:831763/FULLTEXT01.pdf (retrieved December 8, 2017)

[99] Wrobel, J., Hoyt, R., Cushing, J., Jaster, M., Voronka, N., Slostad, J., Paritsky, L., ‘Versatile Structural Radiation Shielding and Thermal Insulation through Additive Manufacturing’ [online]

https://digitalcommons.usu.edu/cgi/viewcontent.cgi?referer=https://www.google.ca/&httpsredir=1&article=2926&context=smallsat (retrieved December 8, 2017)

[100] Andre, N., Blanc, M., Maurice, S., Schippers, P., Pallier, E., Gombosi, T., Hansen, K., Young, D., Crary, F., Bolton, S., Sittler, E., Smith, H., Johnson, R., Baragiola, R., Coates, A., Rymer, A., Dougherty, M., Achilleos, N., Arridge, C., Krimigis, S., Mitchell, D., Krupp, N., Hamilton, D., Dandouras, I., Gurnett, D., Kurth, W., Louarn, P., Srama, R., Kempf, S., Waite, H., Esposito, L., Clarke, J., 'Identification of Saturn's Magnetospheric Regions and Associated Plasma Processes: Synopsis of Cassini Observations during Orbit Insertion', *Reviews of Geophysics, 46*, 31 December 2008, doi: 10.1029/2007RG000238

[101] NewSpace Systems CubeSat Magnetorquer Rod [online] https://www.isispace.nl/brochures/NSS_Cubesat_Magnetorquer_Rod_2a-.pdf (accessed 14 January 2017)

[102] Space Micro Miniature Integrated Star Tracker (MIST) [online] http://www.spacemicro.com/assets/datasheets/guidance-and-nav/MIST.pdf (accessed 14 January 2017)

[103] NewSpace Systems CubeSat Sun Sensor [online] https://www.isispace.nl/brochures/NSS_Cubesat_Sun_Sensor_2a-.pdf (accessed 14 January 2017)

[104] Hajos, G., Jones, J., Behar, A., 'An Overview of Wind-Driven Rovers for Planetary Exploration', [online] http://citeseerx.ist.psu.edu/viewdoc/download?doi=10.1.1.79.6694&rep=rep1&type=pdf (retrieved 13 December 2017)

Appendix A - Sun Position and Solar Insolation from Martian Surface (MATLAB script)

```
% Finds the sun position at a given position and time range on Mars, and
% the solar insolation that results from it
clear all

% Set initial values for latitude and longitude
% Latitude (lat) is 80 degrees and longitude (lon) is 0 degrees
% For this program, all angles are in degrees, and converted to radians by
% multiplying by pi/180
 lat = 80.*pi./180;
 lon = 0.*pi./180;

%% Find number of days since J2000 epoch
% Create a vector of Julian dates from August 25 2021 to February 24 2022
% (Mars year 36)
% Julian Day 2459253 on February 07, 2021 (spring equinox, Ls 0)
% Julian Day 2459452 on August 25, 2021 (summer solstice, Ls 90)
% Julian Day 2459635 on February 24, 2022 (autumnal equinox, Ls 180)
% Julian Day 2459782 on July 21, 2022 (winter solstice, Ls 270)

JD_UT = linspace(2459581,2459582,50);

% Determine time offset from J2000 epoch (UT) in Julian centuries
T = (JD_UT - 2451545.0)/36525.;

% Determine UTC to TT conversion - difference between UTC and TT
difference = 64.184 + (59.0*T) - (51.2*T.^2) - (67.1*T.^3) - (16.4*T.^4);
% T in Julian centuries
% difference is in seconds

% Determine Julian Date (TT)
JD_TT = JD_UT + ((difference)/86400.); % in s/day

% Determine the time offset from J2000 epoch (TT)
deltat = JD_TT - 2451545.0; % in days

%% Determine Martian orbital parameters
% Determine Mars mean anomaly
M = (19.3870 + 0.52402075.*deltat)*pi./180;
```

```
% Determine angle of Fictional Mean Sun
alphaFMS = (270.3863 + 0.52403840.*deltat)*pi./180;

% Determine sum of perturbers
   pert = [0.0071 2.2353 49.409
   0.0057 2.7543 168.173
   0.0039 1.1177 191.837
   0.0037 15.7866 21.736
   0.0021 2.1354 15.704
   0.0020 2.4694 95.528
   0.0018 32.8493 49.095];
PBS = 0;
for i=1:7
   PBS = PBS + (pert(i,1).*cos(((360/365.25).*deltat./pert(i,2)+pert(i,3)).*pi./180)).*pi./180;
end

% Determine Equation of Center (true anomaly minus mean anomaly)
EOC = ((10.691 + 3E-7*deltat).*sin(M) + 0.623.*sin(2.*M) + 0.05.*sin(3.*M) +
0.005.*sin(4.*M) + 0.0005.*sin(5.*M))*pi/180 + PBS;

% Determine areocentric solar longitude
ls = (alphaFMS + EOC);

%% Determine Mars Time
% Determine Equation of Time
EOT = (2.861.*sin(2.*ls)-0.071.*sin(4.*ls)+0.002.*sin(6.*ls)).*pi./180 - EOC;

% The above result for EOT is in radians. 1 hour = 15 degrees = 0.2618 rad.
% Multiply by 1 h/0.2618 radians to obtain the result in hours (EOTh)
EOTh = EOT/0.2618;

% Determine Coordinated Mars Time. This is the mean solar time at Mars'
% prime meridian.
MTC = mod((24.*((JD_TT - 2451549.5)./1.027491252) + 44796.0 - 0.00096),24); % in hours

% Determine Local Mean Solar Time
LMST = mod(MTC - lon.*24./(2.*pi),24); % in hours

% Determine Local True Solar Time
LTST = mod(LMST + EOTh.*(12./pi),24); % in hours

% Determine the subsolar longitude
```

```
subSolarLong = mod(MTC.*pi./12 + EOTh + pi,2.*pi);

%% Additional Calculations
% Determine the planetographic solar declination
deltaS = asin(0.42565.*sin(ls)) + 0.25.*pi./180.*sin(ls);

% Determine heliocentric distance in AU
RM = 1.523679.*(1.00436 - 0.09309*cos(M) - 0.004336*cos(2*M) - 0.00031*cos(3*M) -
0.00003*cos(4*M));

% Determine heliocentric longitude
lM = (ls + 85.061 - 0.015.*sin(71 + 2*ls) - 5.5E-6*deltat)*pi./180;

% Determine heliocentric latitude
bM = -((1.8497 - 2.23E-5*deltat).*sin(ls - 144.5 + 2.57E-6.*deltat))*pi./180;

% Hour angle
H = lon - subSolarLong;

% Determine solar zenith angle
SZA = acos(sin(deltaS).*sin(lat) + cos(deltaS).*cos(lat).*cos(H));

% Determine local solar elevation
LSE = pi/2 - SZA;

% Solar Azimuth
Az = mod(atan2(sin(H),cos(lat).*tan(deltaS) - sin(lat).*cos(H)),2.*pi);

%% Solar Flux
% F0 is flux at top of the Martian atmosphere
% RM is the Sun-Mars distance
 S = 1367; % W/m^2, solar insolation at top of Earth's atmosphere
 a = 1; % semi major axis of Earth, in AU
 F0 = S./((RM./a).^2);

% F is flux in the Martian atmosphere
% Optical depth of 0.3 is used as a baseline
 F = F0.*exp(-0.3./cos(SZA))

% To prevent the flux from blowing up at the horizon, define F = NaN at the
% horizon

for i = 1:length(JD_UT)
```

```
    if(SZA(i)<89.9*pi/180)
        F(i) = F0(i).*exp(-0.3./cos(SZA(i)));
    else
        F(i) = NaN;
    end
end

%% Plot results
% LSE vs. LTST
plot(LTST, LSE)
xlabel('LTST [hours]');
ylabel('LSE [radians]');

% Az vs. LTST
figure(2)
plot(LTST, Az)
xlabel('LTST [hours]');
ylabel('Az [radians]');

% Solar Insolation vs. LTST (at top of atmosphere)
figure(3)
plot(LTST, F0)
xlabel('LTST [hours]');
ylabel('Flux [W/m^2]');

% Solar Insolation vs. LTST (in atmosphere)
figure(4)
plot(LTST, F)
xlabel('LTST [hours]');
ylabel('Flux [W/m^2]');
```

Appendix B - Rendezvous Delta-V around Saturn (MATLAB Script)

```
% Finds the delta-V of a rendezvous between mothership A and small
% spacecraft B around Saturn

clear all
clc
%{
  This script uses the state vectors of mothership A and small spacecraft B
  to find the delta-V of a rendezvous

  rA,vA     - state vector of A (km, km/s)
  rB,vB     - state vector of B (km, km/s)
  hA        - angular momentum vector of A (km^2/s)
  i, j, k   - unit vectors along the x, y and z axes of A's
              LVLH frame
  QXx       - DCM of the LVLH frame relative to the kronocentric
              equatorial frame (KEF)
  Omega     - angular velocity of the LVLH frame (rad/s)
  Omega_dot - angular acceleration of the LVLH frame (rad/s^2)
  aA, aB    - absolute accelerations of A and B (km/s^2)
  r_rel     - position of B relative to A in KEF (km)
  v_rel     - velocity of B relative to A in KEF (km/s)
  a_rel     - acceleration of B relative to A in KEF (km/s^2)
  r_rel_x   - position of B relative to A in the LVLH frame
  v_rel_x   - velocity of B relative to A in the LVLH frame
  a_rel_x   - acceleration of B relative to A in the LVLH frame

%}

% Small spacecraft B is at 0 degrees inclination (equatorial orbit).
% Mothership A is slightly above this inclination (1 degree or less)

mu = 37931000; % km3/s2, Curtis Table A.2
deg = pi/180;

%% Angle of Orbit to Ring Plane

s = 0.3; % vertical distance of mothership from ring plane, km
r = 74000; % km

   %% Parameters of A
   r_A   = r;
```

```
   e_A    = (r_A - r_A)/(r_A + r_A);
   RA_A   = 20*deg;
   theta  = atand(s/r_A); % degrees
   incl_A = theta*deg; % radians
   w_A    = 0*deg;
   TA_A   = 60*deg;
   h_A    = sqrt(r_A*mu*(1+e_A*cos(TA_A)));

   T_A = (((2*pi)/sqrt(mu))*((2*r_A)/2)^1.5)/3600; % period, in hours

   %% Parameters of B
   r_B1   = r_A;
   r_B2   = r_A;
   e_B    = (r_B2 - r_B1)/(r_B2 + r_B1);
   RA_B   = 20*deg;
   incl_B = 0*deg;
   w_B    = 0*deg;
   TA_B   = 60*deg;
   h_B    = sqrt(r_B1*mu*(1+e_B*cos(TA_B)));

   T_B = (((2*pi)/sqrt(mu))*((r_B1+r_B2)/2)^1.5)/3600; % period, in hours
%{
("kronocentric" is Saturn-centric in this context)
  R3_w - Rotation matrix about the z-axis through the angle w
  R1_i - Rotation matrix about the x-axis through the angle i
  R3_W - Rotation matrix about the z-axis through the angle RA
  Q_pX - Matrix of the transformation from perifocal to kronocentric equatorial frame
  rp   - position vector in the perifocal frame (km)
  vp   - velocity vector in the perifocal frame (km/s)
  r    - position vector in the kronocentric equatorial frame (km)
  v    - velocity vector in the kronocentric equatorial frame (km/s)
%}

%% Find rA and vA with Algorithm 4.5 (requires angular elements be in radians):
% Equations 4.45 and 4.46 (rp and vp are column vectors):
rp_A = (h_A^2/mu) * (1/(1 + e_A*cos(TA_A))) * (cos(TA_A)*[1;0;0] + sin(TA_A)*[0;1;0]);
vp_A = (mu/h_A) * (-sin(TA_A)*[1;0;0] + (e_A + cos(TA_A))*[0;1;0]);

% Equation 4.34:
R3_W_A = [ cos(RA_A)  sin(RA_A)  0
       -sin(RA_A)  cos(RA_A)  0
           0        0     1];
```

```
% Equation 4.32:
R1_i_A = [1       0          0
       0   cos(incl_A)  sin(incl_A)
       0  -sin(incl_A)  cos(incl_A)];

% Equation 4.34:
R3_w_A = [ cos(w_A)  sin(w_A)  0
       -sin(w_A)  cos(w_A)  0
          0       0     1];

% Equation 4.49:
Q_pX_A = (R3_w_A*R1_i_A*R3_W_A)';

% Equations 4.51 (rA and vA are column vectors):
rA = Q_pX_A*rp_A;
vA = Q_pX_A*vp_A;

% Convert rA and vA into row vectors:
rA = rA';
vA = vA';

%% Find rB and vB with Algorithm 4.5 (requires angular elements be in radians):
% Equations 4.45 and 4.46 (rp and vp are column vectors):
rp_B = (h_B^2/mu) * (1/(1 + e_B*cos(TA_B))) * (cos(TA_B)*[1;0;0] + sin(TA_B)*[0;1;0]);
vp_B = (mu/h_B) * (-sin(TA_B)*[1;0;0] + (e_B + cos(TA_B))*[0;1;0]);

% Equation 4.34:
R3_W_B = [ cos(RA_B)  sin(RA_B)  0
       -sin(RA_B)  cos(RA_B)  0
          0       0     1];

% Equation 4.32:
R1_i_B = [1       0          0
       0   cos(incl_B)  sin(incl_B)
       0  -sin(incl_B)  cos(incl_B)];

% Equation 4.34:
R3_w_B = [ cos(w_B)  sin(w_B)  0
       -sin(w_B)  cos(w_B)  0
          0       0     1];

% Equation 4.49:
Q_pX_B = (R3_w_B*R1_i_B*R3_W_B)';
```

```
% Equations 4.51 (rB and vB are column vectors):
rB = Q_pX_B*rp_B;
vB = Q_pX_B*vp_B;

% Convert rB and vB into row vectors:
rB = rB';
vB = vB';

%% Calculate the relative position, velocity, and acceleration
% Calculate the vector hA:
hA = cross(rA, vA);

% Calculate the unit vectors i, j and k:
i = rA/norm(rA);
k = hA/norm(hA);
j = cross(k,i);

% Calculate the transformation matrix QXx:
QXx = [i; j; k];

% Calculate Omega and Omega_dot:
Omega     = hA/norm(rA)^2;                % Equation 7.5
Omega_dot = -2*dot(rA,vA)/norm(rA)^2*Omega;% Equation 7.6

% Calculate the accelerations aA and aB:
aA = -mu*rA/norm(rA)^3;
aB = -mu*rB/norm(rB)^3;

% Calculate r_rel:
r_rel = rB - rA;

% Calculate v_rel:
v_rel = vB - vA - cross(Omega,r_rel);

% Calculate a_rel:
a_rel = aB - aA - cross(Omega_dot,r_rel)...
      - cross(Omega,cross(Omega,r_rel))...
      - 2*cross(Omega,v_rel);

% Calculate r_rel_x, v_rel_x and a_rel_x:
r_rel_x = QXx*r_rel';
v_rel_x = QXx*v_rel';
```

```
a_rel_x = QXx*a_rel';

%% C-W matrices

n = norm(vA)/r_A; % mean motion of mothership, rad/s
t = 2*3600; % number of hours

phi_rr = [ 4 - 3*cos(n*t)  0  0
       6*(sin(n*t) - n*t)  1  0
         0      0    cos(n*t)];

phi_rv = [ (1/n)*(sin(n*t))  (2/n)*(1 - cos(n*t))  0
       (2/n)*(cos(n*t) - 1)  (1/n)*(4*sin(n*t) - (3*n*t))  0
         0      0    (1/n)*sin(n*t)];

phi_vr = [ 3*n*sin(n*t)  0  0
       6*n*(cos(n*t) - 1)  0  0
         0      0    -n*sin(n*t)];

phi_vv = [ cos(n*t)  2*sin(n*t)  0
       -2*sin(n*t)  4*cos(n*t)-3  0
         0      0    cos(n*t)];

dv0_plus = -inv(phi_rv)*phi_rr*r_rel_x;
dvf_neg = (phi_vr*r_rel_x) + (phi_vv*dv0_plus);

%% Plane Change Delta-V and Propellant
% delta-V needed to make a plane change from plane A to plane B
% Need first to find the radial and azimuthal velocities of spacecraft A

v_az = (mu/h_A)*(1 - e_A*cos(TA_A));
v_r = (mu/h_A)*(e_A*sin(TA_A));
v = sqrt((v_az^2) + (v_r^2));

delta = incl_A - incl_B;
deltaVplane = (2*v*sin(delta/2))*1000; % m/s (multiplied by 1000 to get m/s, otherwise km/s)

%% Rendezvous Delta-Vs
% Delta-V at beginning of rendezvous maneuver
deltaV0 = dv0_plus + v_rel_x;
Vstart = norm(deltaV0);

% Delta-V at end of rendezvous maneuver
```

```
dvf_plus = [0;0;0];
deltaVf = dvf_plus - dvf_neg;
Vend = norm(deltaVf);

% Total Delta-V requirement
deltaVtotal = Vstart + Vend; % km/s
deltaVtotal = deltaVtotal*1000; % m/s
%deltaVtotal = 0.0364;
%% Propulsion
Isp = 1700; % specific impulse, seconds
g = 9.807; % gravitational acceleration on Earth, m/s^2
mass = 10; % spacecraft mass, kg
thrust = 800e-6; % Newtons

% impulsive thrust
mfraction = exp(deltaVtotal/(Isp*g)); % mass fraction of spacecraft (initial mass divided by final
mass)
pfraction = 1 - exp(-deltaVtotal/(Isp*g)); % propellant mass fraction
propmass = mass*pfraction; % propellant mass, kg

% non-impulsive thrust
m_dot = thrust/(Isp*g); % kg/s
burntime = propmass/m_dot; % seconds
burntime = burntime/60; % minutes
```